Cement and Concrete Research 196 (2025) 107942

Contents lists available at ScienceDirect

Cement and Concrete Research

journal homepage: www.elsevier.com/locate/cemconres

Durability of cementitious binders with blast furnace slag in deep sea conditions: Analysis of microstructure and phase transformation

Keisuke Takahashi [a,b,*,1], Yuichiro Kawabata [c,d], Mari Kobayashi [b], Takafumi Kasaya [e], Shintaro Miyamoto [f], Hong S. Wong [g]

[a] Innovation Design Institute, Kagawa University, Japan
[b] Research and Development Center, Mitsubishi UBE Cement Corporation, Japan
[c] Structural Engineering Department, Port and Airport Research Institute, Japan
[d] Research Center for Green X-Tech, Tohoku University, Japan
[e] Research Institute for Marine Resources Utilization Submarine Resources Research Center, Japan Agency for Marine-Earth Science and Technology, Japan
[f] Graduate School of Engineering Department of Civil and Environmental Engineering, Tohoku University, Japan
[g] Department of Civil and Environmental Engineering, Imperial College London, United Kingdom

ARTICLE INFO

Keywords:
Blast furnace slag cement
Deep-sea durability
Seawater ingress
Ettringite formation
Decalcification
Hydrotalcite-like phases
Hydraulic pressure

ABSTRACT

Portland cement-blast furnace slag (PC-BFS) cement-based materials exhibit good durability in shallow marine environments but their performance in the deep-sea is poorly understood. This study investigates the degradation of PC-BFS cement pastes after one-year exposure in a deep-sea field site under high hydraulic pressure (3515 m depth) and low temperature (2 °C) conditions. The results show that the main degradation mechanisms involve ettringite formation and Ca leaching, driven by low-temperature seawater ingress under pressure. SEM-EDS and XRD analyses revealed distinct microstructural changes such as Mg and Al enrichment and sulfate/chloride incorporation in BFS rims. Fluorescence imaging confirmed complete seawater infiltration, facilitating BFS dissolution and reprecipitation cycles. The findings highlight the vulnerability of PC-BFS systems to ettringite-induced damage due to their high alumina and low sulfate balance. These insights inform strategies to optimise cementitious materials for deep-sea applications under extreme environments.

1. Introduction

Blast furnace slag (BFS) cement is widely recognized as an excellent binder for durable concrete structures [1–5], particularly in marine environments where chloride-induced corrosion of reinforcing steel is the primary cause of deterioration. The addition of BFS enhances the durability of concrete by densifying its microstructure through hydration and pozzolanic reaction [6,7], and increasing the formation of AFm phases capable of binding chloride ions [8,9]. A reduction in chloride diffusivity occurs with the microstructure densification and decrease in Ca/Si ratio [10]. Field exposure experiments have demonstrated that concretes made from BFS cement exhibit lower chloride ion ingress compared to ordinary Portland cement (PC) concrete after only several months in seawater and the difference becomes much larger over decades [11].

However, the mechanisms of seawater-induced deterioration in deep-sea environments (depths >200 m) differ significantly from those in shallow sea conditions. Previous investigations by the authors into the durability of PC [12] and calcium aluminate cement systems in deep-sea conditions [13,14] indicated that key factors accelerating deterioration include Ca leaching and phase changes driven by low-temperature seawater [15]. Additionally, high hydraulic pressure drives water ingress, leading to strain-induced cracking [16–19] and increased penetration of ionic species [20,21]. In the initial stages of water ingress, the coexistence of saturated and unsaturated regions has been found to enhance the mechanical properties of the material [22]. Low temperatures further amplify mass transfer by accelerating calcium hydroxide (CH) leaching [23] and subsequent microstructure coarsening [15]. For example, the saturation concentration of Ca^{2+} ions in CH increases approximately 10 % at 2 °C compared to 20 °C [24]. Furthermore, the

* Corresponding author at: Innovation Design Institute, Kagawa University, Japan.
E-mail addresses: takahashi.keisuke@kagawa-u.ac.jp (K. Takahashi), kawabata-y@p.mpat.go.jp (Y. Kawabata), mari.kobayashi@mu-cc.com (M. Kobayashi), tkasa@jamstec.go.jp (T. Kasaya), shintaro.miyamoto.b8@tohoku.ac.jp (S. Miyamoto), hong.wong@imperial.ac.uk (H.S. Wong).
[1] Postal address: 4–8-27 Ban-cho, Takamatsu 7,600,017 Japan.

https://doi.org/10.1016/j.cemconres.2025.107942
Received 7 March 2025; Received in revised form 7 May 2025; Accepted 16 May 2025
Available online 22 May 2025
0008-8846/© 2025 The Authors. Published by Elsevier Ltd. This is an open access article under the CC BY license (http://creativecommons.org/licenses/by/4.0/).

solubility of ettringite decreases at low temperatures. For example, its solubility at 5 °C is approximately 100 times lower than at 20 °C, leading to increased precipitation and associated microstructural damage [25].

PC-BFS cement-based systems may experience unique deterioration mechanisms in the deep-sea environment due to their higher alumina content and increased ettringite formation, compared to PC -based systems [12,15]. For example, a previous study [26] on lightweight aggregate concretes containing BFS cement exposed to low-temperature marine environment revealed increased surface scaling in samples with higher BFS contents, which suggests an earlier onset of seawater-induced deterioration. However, there are many open questions concerning the performance of cementitious materials in the deep-sea. Predicting degradation in deep seawater environments using phase equilibrium calculations remains challenging due to the lack of thermodynamic data for these conditions [15]. Experimental data obtained under actual environmental conditions are, therefore, essential for advancing the understanding of these degradation mechanisms.

To address these challenges, the authors have been conducting long-term field exposure and performance monitoring of various cement-based materials at a seawater depth of 3515 m since 2018. The specimens include hardened cement pastes derived from PC blended with BFS, fly ash, metakaolin, silica fume, and calcium aluminate cement [27,28]. Interestingly, the PC-BFS system exhibited the most severe deterioration, as evidenced by visual observations of surface scaling, despite its well-known performance in shallow marine environments.

This study aims to elucidate the deterioration mechanisms of PC-BFS cement-based materials in deep-sea environments by examining their phase composition and microstructural changes, and by comparing their behaviour when exposed to low- and ambient-temperature seawater at atmospheric pressure as a reference, and water ingress under hydraulic pressure. The performance of other cement systems will be the subject of future publications. This study specifically focuses on PC-BFS, as it exhibited the most severe deterioration and the greatest divergence from the reference samples. We envisage that the findings will provide critical insights into the performance of BFS cement-based materials under extreme conditions and lay a foundation for the development of more durable infrastructure materials suitable for deep-sea and cold marine regions, and deep underground applications.

2. Experimental program

2.1. Materials and sample preparation

The cementitious binder used in this study was a mixture of high-early-strength PC conforming to JIS R 5210 and BFS conforming to JIS A 6206. The chemical compositions of PC and BFS, determined by X-ray fluorescence, are shown in Table 1. The PC contained no limestone powder. The BFS used in the experiment consisted of 3.5 % gypsum and 96.5 % glass phase determined by X-ray diffraction (XRD) Rietveld method. The basicity of BFS, calculated from its chemical composition (Table 1), was 1.92. The Blaine specific surface area, measured according to JIS R 5201, was 4450 cm^2/g for PC and 4090 cm^2/g for BFS.

A PC-BFS blended cement paste was prepared. The BFS replacement ratio was 45 %, corresponding to Type B slag cement as defined by JIS R 5211 (equivalent to CEM II). The blended cement paste will be referred to as "BFS45" in this paper. The water-to-binder (w/b) mass ratio was set at 0.60 to compare with our previous studies [12,15], which is below the upper limit of 0.65 recommended by the Overseas Coastal Area Development Institute of Japan [29] for non-reinforced concrete structures. To prevent segregation in the paste during mixing, a hydroxypropyl methylcellulose (HPMC) thickener was added at 0.13 wt% binder. Air content was controlled between 3 % and 5 % by incorporating a propylene oxide-based defoamer at 0.017 wt% binder.

The paste was mixed for 3 min at 1100 rpm using a hand-held mechanical mixer and cast into cylindrical moulds with dimensions of 50 mm in diameter and 100 mm in height. The specimens were sealed with polyvinylidene chloride film and cured for three months in a constant-temperature chamber at 20 °C. After curing, the top and bottom 5 mm of the specimens were trimmed using a bench saw to remove surface heterogeneities. The side surfaces of the specimens were coated with a water-impermeable epoxy resin to allow seawater ingress to occur exclusively through the top and bottom surfaces during exposure.

The reaction degree of BFS, determined by selective dissolution after three-month curing, was 0.60. Selective dissolution was conducted in accordance with JSCE-D 501–2018, using an EDTA-triethanolamine solution to quantify the undissolved residues of the hardened paste. The dissolution residue was corrected for the contributions from PC and BFS phases. The volume percentages of hydrate phases in the BFS45 paste before seawater exposure, calculated using thermodynamic equilibrium modelling (assuming all PC was hydrated) were 52.4 % calcium silicate hydrate (C-S-H), 4.3 % portlandite, 28.6 % monosulfate and 4.0 % hydrotalcite (hydroxide-type) and 10.7 % unreacted BFS. Additional details of the calculation are provided in Appendix A1.

2.2. Exposure conditions

2.2.1. Deep-sea field exposure

Paste specimens were placed on the seafloor at a depth of 3515 m in a deep-sea experimental field facility and retrieved after 361 days of exposure. This was carried out using the deep-submergence research vehicle (DSV) Shinkai 6500 [30] on the S/V Yokosuka cruises YK22-09C [27] and YK23-08C [28] in May 2022 and 2023, respectively. The facilities are owned and operated by the Japan Agency for Marine-Earth Science and Technology (JAMSTEC). The deep-sea experimental field site is located at the northern edge of the Nankai Trough off Suruga Bay, Shimizu, Japan. The site maintains stable seawater conditions with a temperature of 1.5 °C, salinity of 35 PSU, and dissolved oxygen levels of 3.1 mL/L. These values represent the averages recorded by the conductivity, temperature, and depth meter on the DSV during the dives. The experimental field is near the carbonate compensation depth (CCD) in the Nankai Trough, which is ~3400 m [31], where carbonates become undersaturated [32]. Fig. 1 shows in-situ photographs of the deep-sea experimental field site and specimens taken after 361 days of exposure.

2.2.2. Laboratory test chamber

As a comparison to the deep-sea exposure condition, replicate paste specimens were immersed in two laboratory-scale seawater tanks (216 L) at atmospheric pressure (0.1 MPa). The seawater temperature in the first tank was maintained at a low temperature of 2 ± 1 °C using a heat exchanger to mimic deep-sea condition. In the second tank, the seawater temperature was allowed to fluctuate between 11 °C and 25 °C,

Table 1
Composition of PC, BFS, and the blended binder used in the BFS45 paste.

Binder	Oxide composition (%)								Loss on ignition (%)
	SiO_2	Al_2O_3	Fe_2O_3	CaO	MgO	SO_3	Na_2O	K_2O	
PC	20.1	5.36	2.73	65.2	0.95	3.04	0.26	0.32	1.17
BFS	32.5	14.3	0.21	42.0	6.09	1.62	0.19	0.25	0.76
BFS45	25.7	9.37 (6.80)	1.60	54.8	3.26	2.40	0.23	0.29	0.99

NOTE: Al_2O_3 content accounting for a 60 % BFS reaction is given in parentheses.

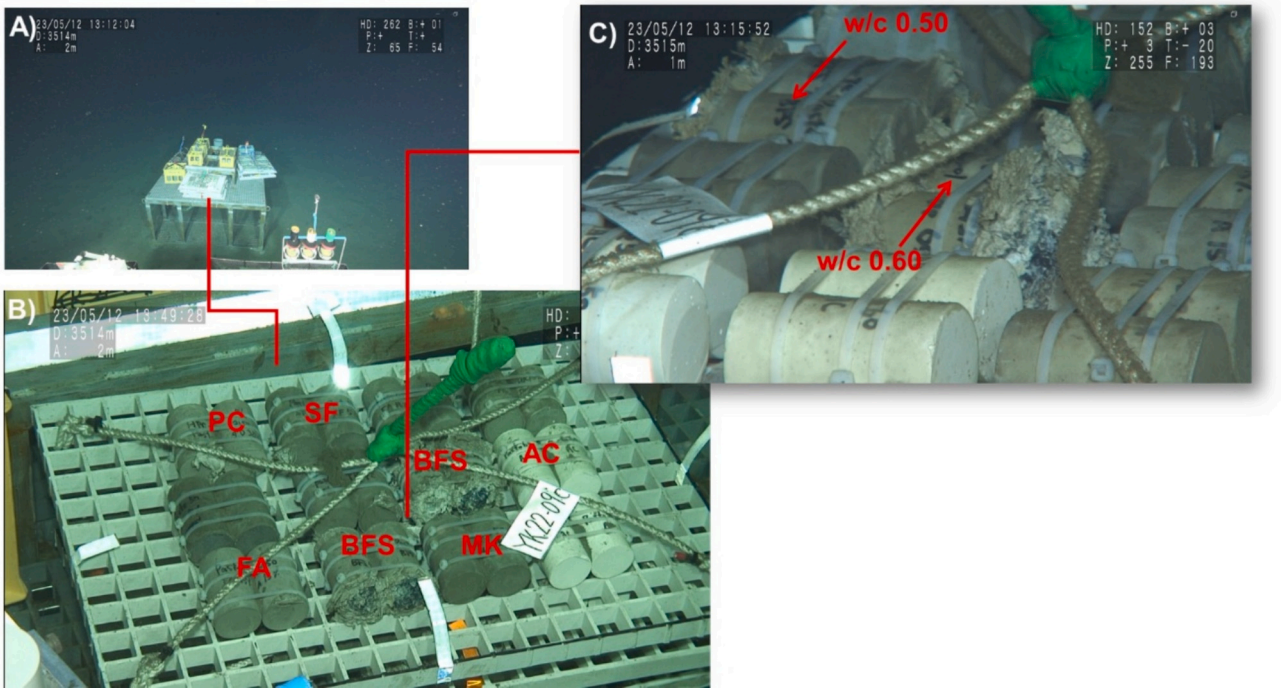


Fig. 1. A) Deep-sea experimental field site at 3515 m depth, located in the Nankai Trough. B) Exposed paste specimens with various cementitious binders including PC, PC blended with 45 % BFS, 15 % fly ash (FA), 15 % metakaolin (MK), 5 % silica fume (SF) and calcium aluminate cement (AC). The w/b of the specimens were 0.50 and 0.60. C) BFS45 specimens are indicated by red arrows. Photographs courtesy of the Japan Agency for Marine–Earth Science and Technology (JAMSTEC). (For interpretation of the references to colour in this figure legend, the reader is referred to the web version of this article.)

according to changes in the ambient temperature during the one-year exposure period. Fresh seawater from a shallow coastal area near the laboratory was supplied to each tank at a flow rate of 150 mL/min and was replaced approximately every 24 h. The salinity of the seawater was consistently measured at around 32 PSU, as reported in [33].

2.3. Test methods

2.3.1. Sample preparation

After the one-year exposure period, specimens were examined using scanning electron microscopy with energy dispersive X-ray spectroscopy (SEM-EDS) and X-ray diffraction (XRD) analyses. The specimens were encased in epoxy first, then sectioned using a table bench saw and a low-speed cutter (IsoMet Precision Cutter, Buehler). Liquid paraffin was used as a lubricant during the cutting process. The samples were sliced to dimensions of approximately 4 cm × 2 cm with a thickness of 1 cm. The sliced samples were subjected to solvent exchange using isopropanol for 30 min at minus 0.1 MPa (absolute pressure of 0.0 MPa), followed by drying in a nitrogen-purged chamber at 20 °C to avoid carbonation and to minimise drying-induced changes to the microstructure. Two replicate samples were examined for statistical significance.

For XRD analysis, approximately 1 g from the sliced samples were milled to a particle size of <90 μm using an agate mortar and pestle in CO_2 free environment. The sampling was carried out at depths of 0–2 mm, 4–6 mm and 10–20 mm from the surface. However, it should be noted that specimens retrieved from the deep-sea exposure site exhibited severe degradation resulting in the loss of approximately 8 mm from the original top and bottom surfaces. Therefore, the apparent surface layer of the deep-sea specimens corresponds to a depth of approximately 8 mm from the original surface of the specimens.

For SEM-EDS analysis, the sliced samples were fully impregnated with low-viscosity epoxy resin following the procedure described in [34]. Once the resin had hardened, the surface of the specimens was polished using diamond powder at progressively smaller particle size down to a 1 μm surface finish. The polished surfaces were then sputter coated with platinum to enhance conductivity and avoid charging effects during SEM observation.

The pretreatment workflow is illustrated in Fig. 2.

2.3.2. XRD

XRD patterns of the powdered samples were obtained using a second-generation D2 PHASER diffractometer (Bruker AXS) equipped with Cu Kα radiation (λ = 1.54 Å) in θ–2θ mode. The XRD was operated at a voltage of 30 kV and a current of 10 mA. The samples were scanned across a 2θ range from 5° to 50°, at step size of 0.02°/min and scanning rate of 2.4°. Phase identification was performed using TOPAS software (Bruker AXS).

2.3.3. SEM-EDS

Microstructure characterisation was carried out on the flat polished epoxy impregnated samples using a JSM-IT-300 scanning electron microscope (JEOL Ltd.) equipped with a backscattered electron (BSE) detector and an energy-dispersive X-ray spectrometer (EDS). BSE imaging and EDS spot analyses were carried out at an accelerating voltage of 15 kV and a working distance of 10.0 mm, under vacuum. High-resolution BSE images were captured to analyse macro- and microstructural features. The magnifications used were 500× and 1500×, with an image size of 5120 × 3840 pixels and resolution ranging from 0.01 to 0.05 μm per pixel.

2.3.4. Fluorescence imaging of water penetration

Water penetration tests were performed on replicate paste specimens that have been sealed cured for three months at 20 °C. The side surfaces were coated with epoxy resin to restrict water penetration to the top and bottom surfaces. Water penetration was conducted under ambient (0.1 MPa) and high-pressure environments (35 MPa), and visualized using a fluorescent tracer solution method [35]. The tracer solution was prepared by diluting fluorescein sodium (1 wt%) with tap water.

For penetration under ambient pressure (0.1 MPa) condition, specimens were submerged in the fluorescent solution inside a sealed plastic

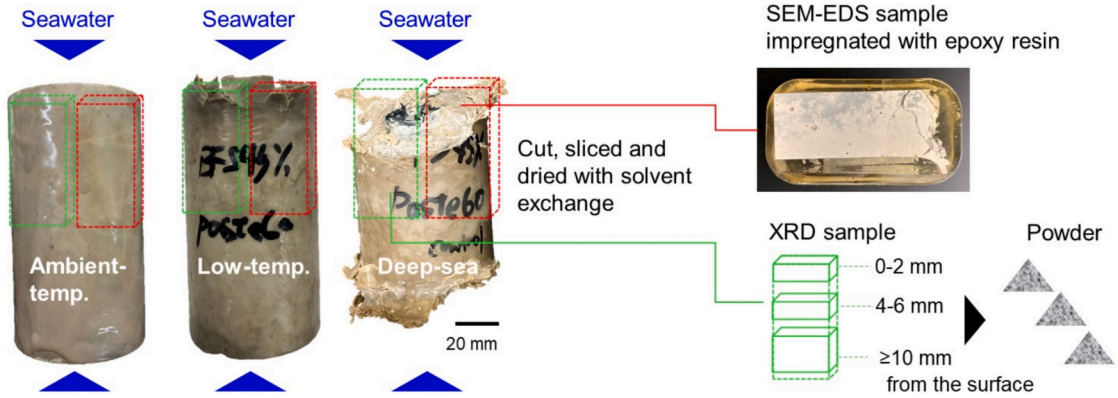


Fig. 2. Exposure conditions and sample pretreatment. Replicate BFS45 specimens were kept in laboratory-scale seawater tanks at either ambient temperature (11–25 °C) or low temperature (1–3 °C) at atmospheric pressure, or in deep-sea field site (1.5 °C) at 3515 m depth for one year, then retrieved and analysed with SEM-EDS and XRD.

bag at a solid-to-liquid volume ratio of approximately 3. For the high-pressure condition, specimens were submerged in a sealed plastic bag filled with the fluorescent solution and then placed in a high-pressure vessel of 4.5 L inner volume [16] maintained at a hydraulic pressure of 35 MPa. The immersion period was set to 12 months for both conditions.

After immersion, specimens were sliced longitudinally using a table bench saw with liquid paraffin as a lubricant. The cross-sections were immediately illuminated with a pair of 6 W ultraviolet lamps in a dark room to induce fluorescence and imaged using a digital camera. Areas where water has penetrated would fluoresce and appear bright yellow/green, allowing measurements to be made. The reproducibility of the test was confirmed through repetitions on three specimens. However, it should be noted that since fluorescein sodium solution has a smaller surface tension (~59 mN/m) than that of seawater (~76 mN/m), the measured penetration depth may slightly overestimate the actual penetration in seawater.

3. Results and discussion

3.1. Visual observation

Fig. 1B and C show the in-situ appearance of specimens at the deep-sea experimental site, hereafter referred to as "deep-sea specimens". All specimens except for those containing calcium aluminate cement (AC) and metakaolin (MK) showed delamination at the top and bottom surfaces, which are in direct contact with seawater (see supplementary material). BFS pastes displayed the most pronounced delamination The degradation caused a loss of up to ~8 mm thick material from the original surface and was significantly more pronounced for specimens with higher w/b ratio. Such deterioration is reminiscent of external sulfate attack, where ingress of sulfate ions promote precipitation of ettringite and other sulfate-bearing phases. The increase in solids volume induces crystallization stress within the pore structure that leads to expansion, cracking and delamination of the exposed surface [36–38].

Upon retrieval and closer inspection, the specimens were observed to have softened, possibly due to ettringite formation, dissolution of CH, and/or leaching of other hydration products. The central undamaged sections of BFS45 displayed a blue-green colour due to the formation of FeS and MnS during hydration, which are expected to oxidize and fade to a grey colour over time [39]. But oxidation did not progress significantly even after one year exposure due to the low dissolved oxygen levels in deep seawater, approximately one-half to one-third of those in shallow seawater at depths exceeding 1000 m [40].

Specimens immersed in the laboratory chamber under atmospheric pressure (0.1 MPa) and 2 °C seawater (hereafter referred to as "low-temp. specimens") also exhibited delamination and a mushy texture. However, degradation was confined to ~2–3 mm from the top surface, as depicted in Fig. 2. The remaining portions retained their original appearance. In contrast, specimens exposed to 0.1 MPa and ambient-temperature seawater (hereafter referred to as "ambient-temp. specimens") showed no signs of deterioration.

Fig. 3 shows example backscattered electron (BSE) images of polished cross-sections at ~0 mm (surface), 5 mm, and 20 mm from the top surface. A dark and dense layer with no visible pores was observed at the surface layer (0 mm) of the deep-sea specimen, which was identified as brucite from EDS analyses. Partially reacted slag can be identified from their angular shaped particles with bright unreacted core surrounded by a dark reaction rim. Unreacted slag particles were almost completely absent at the surface layer of the deep-sea specimens. At 5 mm and 20 mm depths from the surface, unreacted slag particles surrounded by thin reaction rims were sporadically observed. In contrast, unreacted slag particles were still visible at the surface layer (0 mm) of the low-temp. and ambient-temp. specimens. Thus, the appearance and microstructure varied significantly among the three exposure conditions.

3.2. Water penetration

Fig. 4 shows water penetration visualized through fluorescence imaging after one-year exposure under ambient pressure (0.1 MPa) and deep-sea equivalent high-pressure (35 MPa) conditions. At ambient pressure, the fluorescent solution penetrated only 0.5–1 mm from the top and bottom surfaces (arrowed). Note that the faint patches on the internal regions are artefacts from reflections. The shallow penetration suggests minimal seawater ingress into the ambient-temp. specimens after one year exposure. In contrast, the specimen at 35 MPa showed that fluorescent solution had infiltrated its entire thickness.

Additional testing was carried out using X-ray micro-computed tomography (X-μCT) to obtain density contrast images and to support the findings from fluorescence imaging. Details of the work are summarised in Appendix A2. The results (Fig. A5) show that specimens that resisted water ingress for 12 months under ambient pressure allowed water to infiltrate to its centre when subjected to hydraulic pressure of 20 MPa for less than one hour. This indicates that at a depth of 3515 m, equivalent to a pressure of 35 MPa, seawater would have completely infiltrated the specimens not long after the exposure.

3.3. XRD analysis

The XRD results for ambient-temp., deep-sea, and low-temp. specimens, sliced at depths of 0–2 mm, 4–6 mm, and ≥ 10 mm from the surface, are presented in Fig. 5. The detectable crystalline products varied depending on the exposure environment and slicing depth. For example, the deep-sea specimens showed significant CH dissolution and

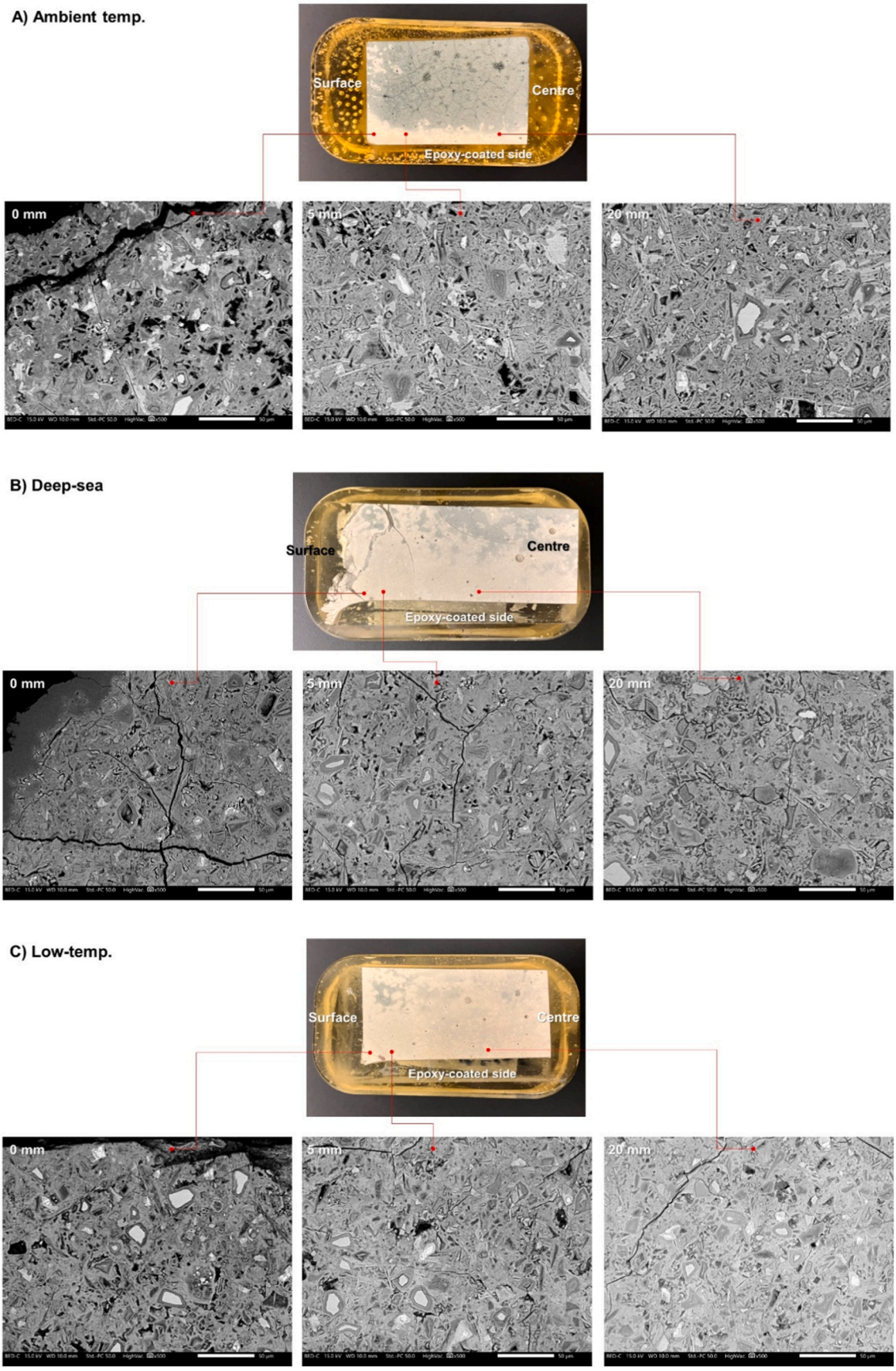


Fig. 3. Polished cross-sections impregnated with epoxy resin for SEM-EDS analysis and example BSE images captured at 0 mm, 5 mm, and 20 mm from the top surface. Note that the 0 mm surface layer of the deep-sea specimen corresponds to a depth of approximately 8 mm from the original surface.

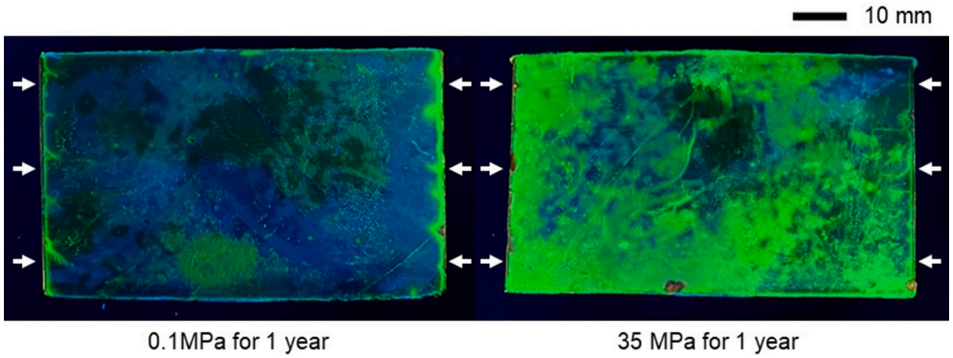


Fig. 4. Water penetration visualized through fluorescence imaging after one year exposure in ambient pressure (0.1 MPa) and high pressure (35 MPa). Arrows indicate direction of penetration.

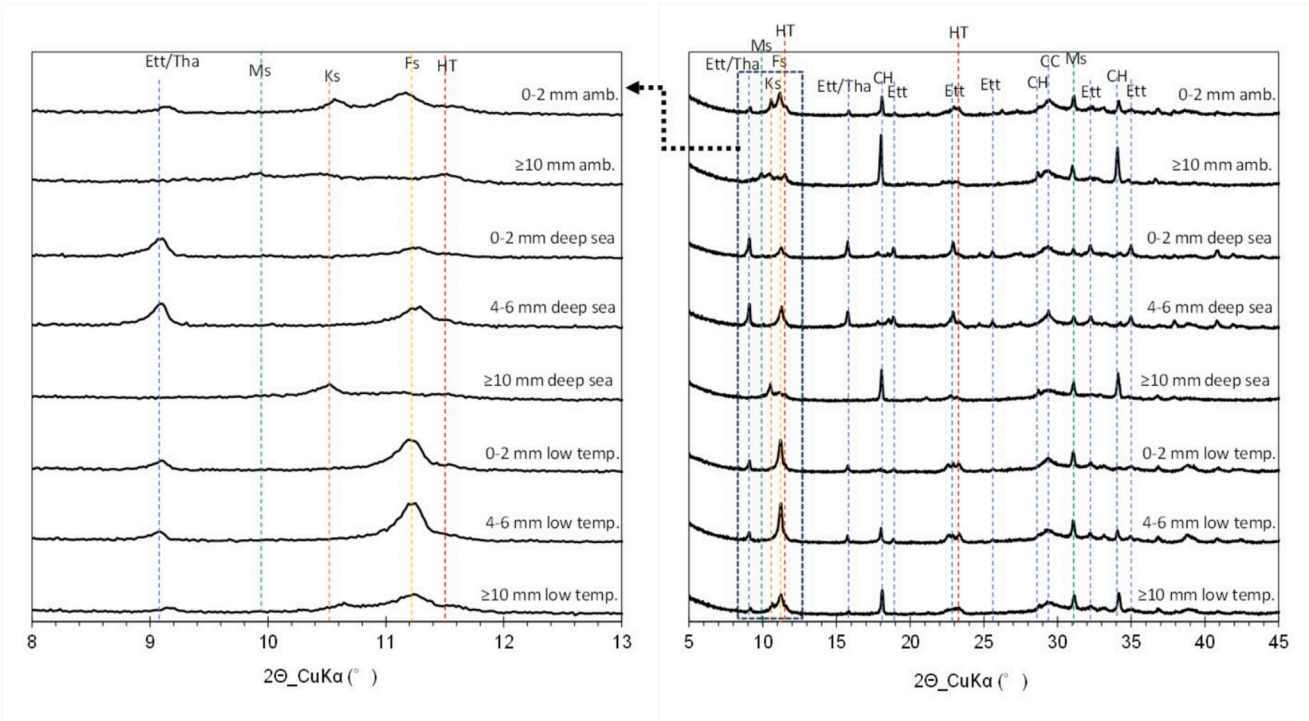


Fig. 5. XRD patterns of ambient-temp., deep-sea and low-temp. specimens sliced at 0–2 mm, 4–6 mm and ≥ 10 mm. Abbreviations: Ett = ettringite, Ms. = monosulfate, Ks = Kuzel's salt, Fs = Friedel's salt, HT = hydrotalcite-like phases [42], CH = portlandite, CC = calcite, Tha = thaumasite. Note that the 0 mm surface layer of deep-sea specimens correspond to a depth of approximately 8 mm from the original surface.

ettringite formation compared to the low-temp. or ambient-temp. specimens. The peaks centred at 2θ = 9° and 16° may be attributed to thaumasite, given its structural similarity to ettringite [41]. However, the corresponding SEM-EDS data did not confirm thaumasite formation within the observed zones, as will be discussed in Section 3.4. Other detectable phases include Kuzel's salt, Friedel's salt and monosulfate. Hydrotalcite-like phases exhibited a characteristic diffraction peak at 11.5° (003 reflection) as mentioned in [41]. These results were used to interpret the SEM-EDS observations in Section 3.4.

3.4. SEM-EDS analysis

3.4.1. Overview

EDS spot analyses were carried out on at least 300 points per specimen, randomly selected within 0–1 mm, 4–6 mm, and 10–20 mm from the surface but avoiding cracks and large voids. The spot analyses were carried out at 500× on bulk paste regions and at a higher magnification of 1500× to focus on BFS grains and their reacted rims. Results are presented as scatter plots of atomic ratios, and compared against the stoichiometric composition of typical hydrates and mineral phases. The hydration of PC-BFS produces calcium alumina silicate hydrate (C-A-S-H), calcium aluminium layered double hydroxides (Ca—Al LDHs), magnesium aluminium layered double hydroxides (Mg—Al LDHs), and nano-sized CH [43]. The stoichiometric composition range for C-A-S-H is set to Si/Ca = 0.55–0.75 and Al/Ca = 0.03–0.15 according to previous studies on PC-BFS systems [44–47]. Unreacted BFS grains have composition in the range of Si/Ca = 0.65–0.85 and Al/Ca = 0.30–0.40 [45,48], while the reaction rim around BFS grains is reported to have a lower composition in the range of Si/Ca = 0.55–0.70 and Al/Ca = 0.15–0.40 [49].

3.4.2. Ambient temperature specimens

Figs. 6 and 7 present the EDS point analysis for the ambient-temp. specimens at 500× and 1500× magnification respectively. Although both figures exhibit broadly similar trends, the plots in Fig. 6 are more influenced by hydrates derived from the reaction of Portland cement.

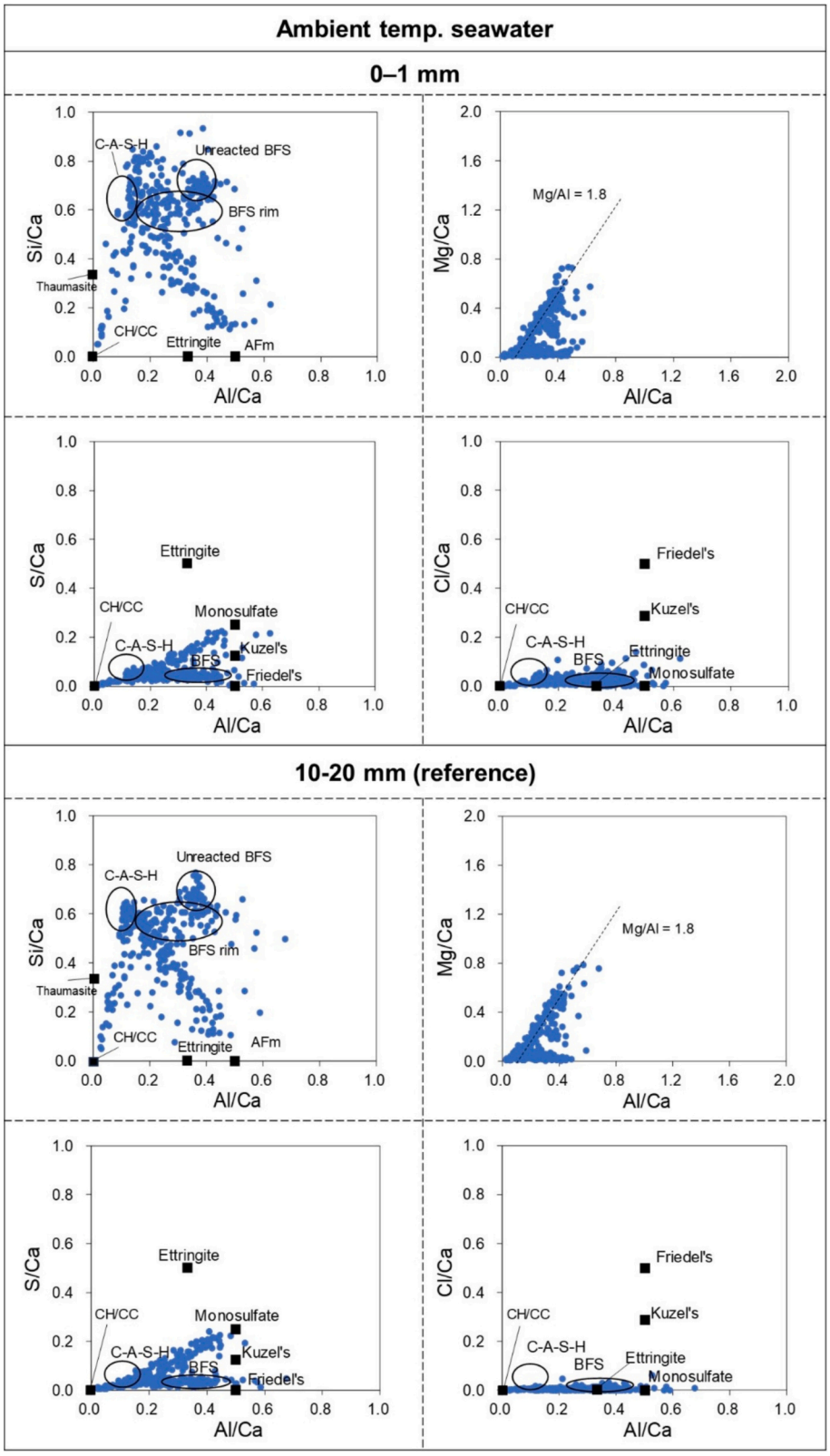


Fig. 6. EDS point analysis of bulk paste in ambient-temp. specimens at 500× magnification.

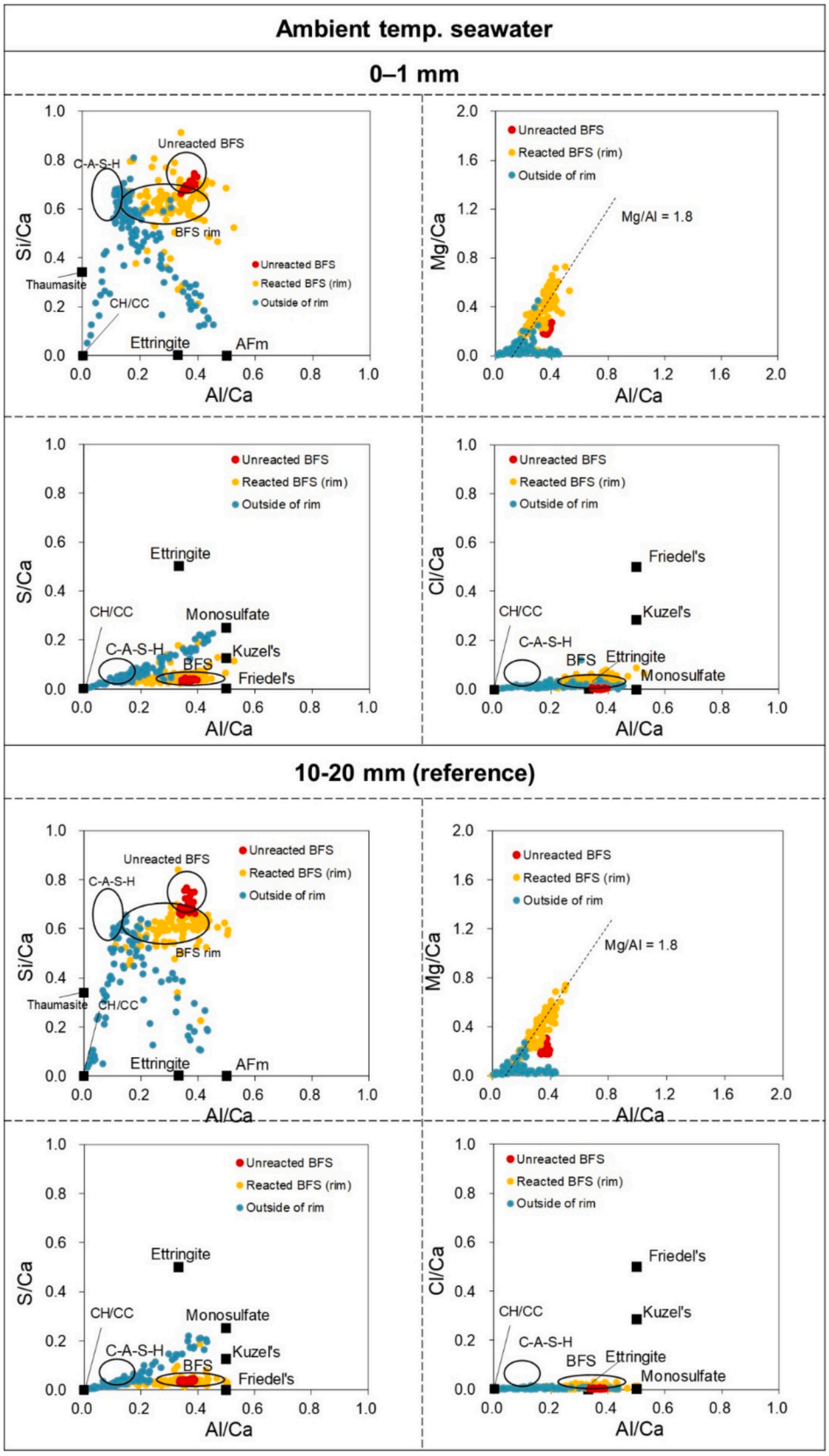


Fig. 7. EDS point analysis of ambient temp. specimens at 1500× magnification.

Results show that the composition at 0–1 mm from the surface was nearly identical to deeper regions (10–20 mm). However, a slight decalcification had occurred, causing the C-A-S-H cluster to shift slightly upward and to the right in the Si/Ca–Al/Ca plot. Additionally, a small amount of chloride uptake was observed in the Cl/Ca–Al/Ca plot, occurring in both the BFS reacted rim and surrounding areas, as shown in Fig. 7. XRD data (Fig. 5) show the formation of Friedel's salt and Kuzel's salt near the surface. No significant changes were observed in the S/Ca or Mg/Ca–Al/Ca plots. Neither Friedel's salt nor Kuzel's salt was detected at 10–20 mm (Fig. 5). These are consistent with the observation that water infiltration was limited to within 1 mm from the specimen surface (Fig. 4).

The Si/Ca–Al/Ca plot in Fig. 6 shows clusters within the C-A-S-H domain, with points aligned with the axis connecting C-A-S-H to AFm, CH/CC (calcite), and BFS rims, indicating mixture of phases. Points located along the line connecting BFS rims and AFm were also observed, suggesting the presence of AFm near or within the BFS rims. AFm was identified as monosulfate, based on the S/Ca–Al/Ca plot in Fig. 6. Mg—Al LDHs precipitate as hydrotalcite-like phases with variable Mg/Al ratio, although the Mg/Al ratio in natural hydrotalcite is typically 3.0 [50]. In hydrated slag systems and slag cement pastes, the Mg/Al ratio has been reported to range between 1.5 and 2.4 [51,52]. In this study, the Mg/Al ratio was ~1.8 based on the slope of the point cluster in the Mg/Ca–Al/Ca plot in Fig. 6.

At 1500× magnification, the BFS grains and their reaction rims reveal differences in grayscale intensity caused by variations in chemical composition and electron density [53,54]. As shown in Fig. 8, unreacted BFS grains are bright and angular, while the surrounding hydrated rim are darker [55,56]. EDS mapping (Fig. 8) showed that the reaction rim had lower Ca and Si content, but higher Mg content, while Al content remained relatively unchanged, compared to unreacted BFS. Outside the rim, Ca content increased, and Mg content decreased. This trend was confirmed in the Mg/Ca–Al/Ca plot from EDS point analysis (Fig. 7).

The reaction rim thickness ranged from 5 to 10 μm. Considering the size of the electron-solid interaction and sampling volume of characteristics X-rays (a few μm at 15 kV [57]), the phase composition of the unreacted BFS, reaction rim, and surrounding areas (10–20 μm beyond the rim) could be evaluated using EDS point analysis. The results (Fig. 7) show that the reaction rim (yellow points) consisted of intermixed Ca—Al LDHs, Mg—Al LDHs, and C-A-S-H, without S or Cl. The area outside the rim (turquoise points) contained mixed CH, C-A-S-H, and monosulfate. These are consistent with previous studies [42,55,56],

3.4.3. Deep-sea specimens

Figs. 9 and 10 present EDS point analysis data for the deep-sea specimens at 500× and 1500× magnification respectively. Results show that the 0–1 mm region had a significantly different composition compared to the undeteriorated reference, taken as the ambient temp. specimen at 10–20 mm. For example, the Si/Ca–Al/Ca plots show a new cluster of points (red-circled) that corresponds to a shift from stoichiometric compositions of C-A-S-H (black-circled) outside the reacted rim. This suggests decalcification of C-A-S-H, a behaviour previously reported in PC pastes and mortars exposed to deep-sea environments [12,15].

Another unique feature in the 0–1 mm region was the presence of data points with Mg/Ca > 0.5 and Al/Ca > 0.5, highlighted yellow in Fig. 9. This indicates an enrichment of hydrotalcite-like phases within the BFS rim, where Ca-free hydrotalcite-like phases became dominant compared to Ca-containing C-A-S-H, leading to relatively higher Mg/Ca and Al/Ca ratios (as shown in the Mg/Ca–Al/Ca plots in Figs. 9 and 10), with Mg/Al ratio remaining at ~1.8. This implies that the rim experienced substantial hydrotalcite-like phase formation, accompanied by decalcification of C-A-S-H as reflected in the scattered distribution of the (yellow) data points. These hydrotalcite-like phases are poorly crystalline or nano crystalline as they did not show distinct peaks in XRD (Fig. 5) [56,58]. The abundance of hydrotalcite-like phases in the 0–1 mm region of the deep-sea specimen is attributed to changes in phase composition and density within the BFS rim and surrounding areas, influenced by low-temperature seawater ingress. This phenomenon is discussed further in Section 3.5.

The S/Ca and Cl/Ca–Al/Ca plots (Figs. 9 and 10) show precipitation of ettringite and Friedel's salt predominantly outside BFS rims. BSE imaging (Fig. 11) and EDS data (Table 2) show two distinct patterns of ettringite precipitation: microscopic ettringite co-precipitated with C-A-S-H forming an intermixed phase, and larger deposits of ettringite crystals that have reprecipitated within cracks and voids. Both patterns

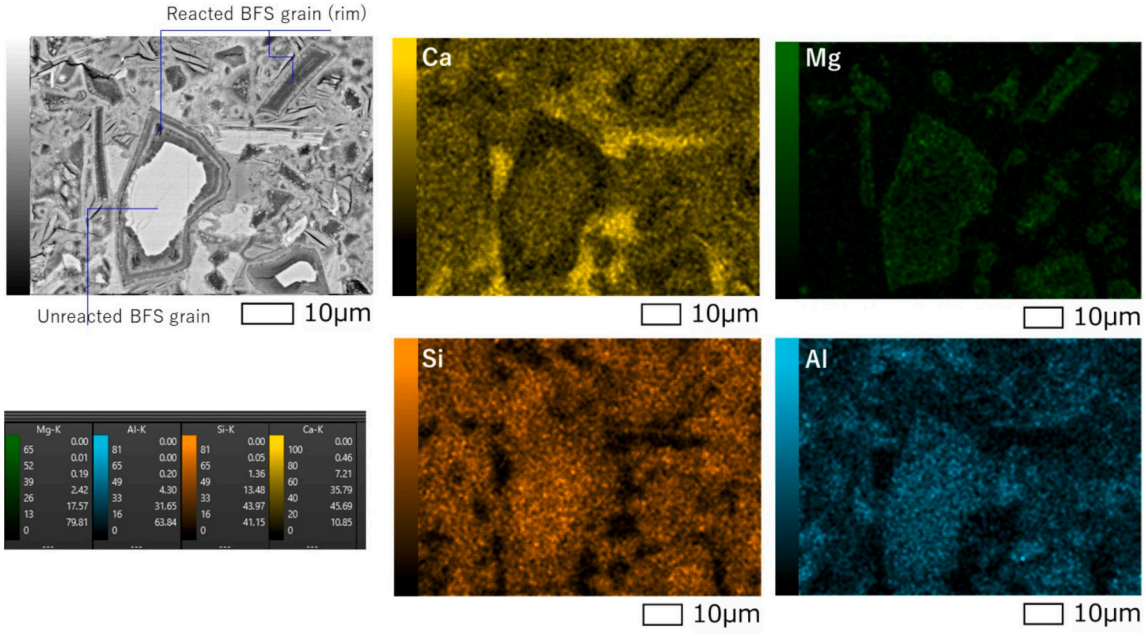


Fig. 8. BSE image and EDS elemental mapping of BFS grains and their surrounding areas at 10–20 mm below the surface in the ambient-temp. specimen (1500 × magnification). The amount of each detected element is displayed on a colour scale normalized to 100 %. The reaction rim showed lower Ca and Si, but higher Mg compared to the unreacted BFS grain. Al content remained relatively constant.

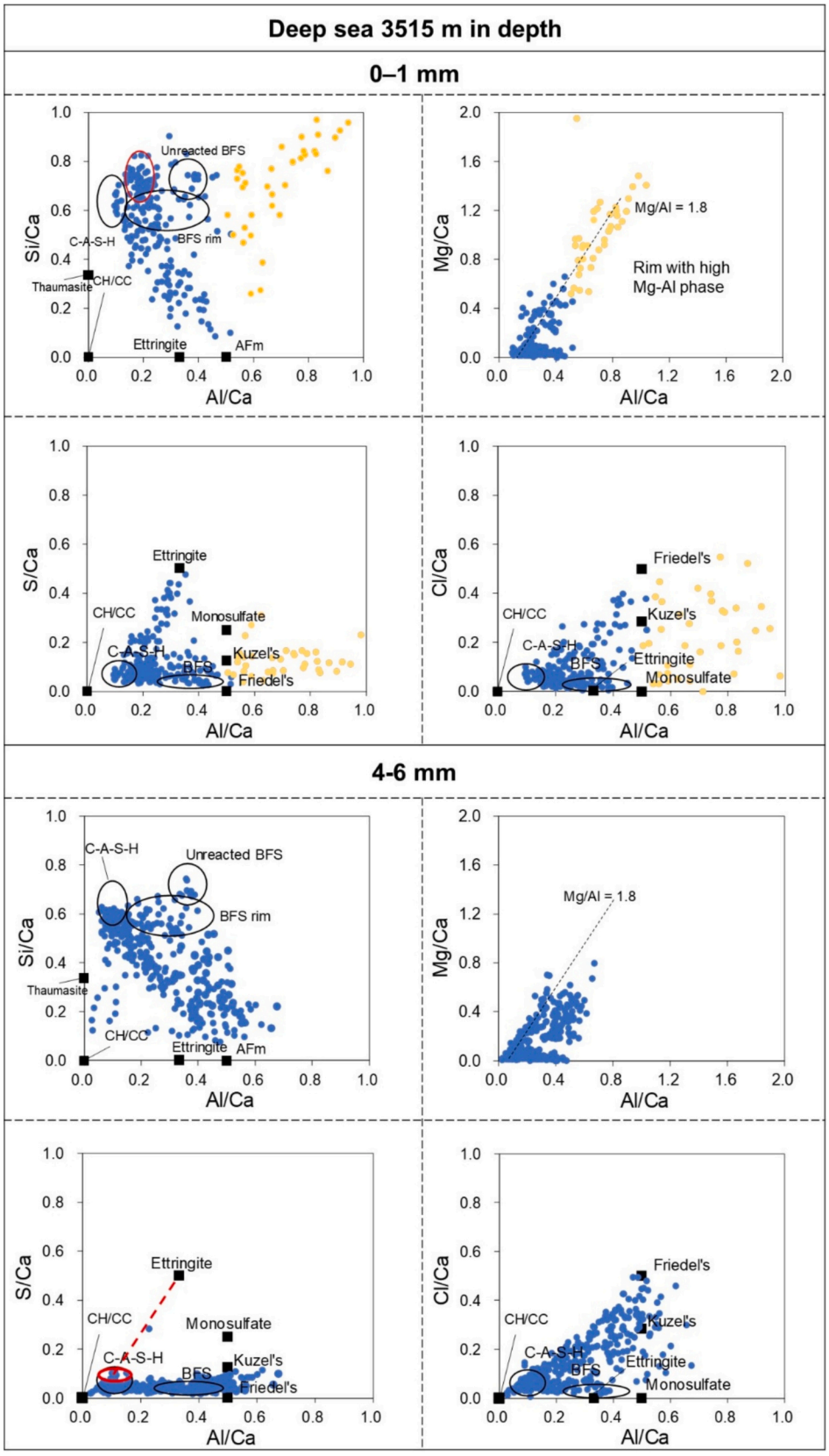


Fig. 9. EDS point analysis of deep-sea specimens at 500× magnification. Points with Al/Ca > 0.5 and Mg/Ca > 0.5 are plotted in yellow. Decalcification of C-A-S-H (red-circled area in the Si/Ca–Al/Ca plot) and ettringite formation within C-A-S-H (red-circled area in the S/Ca–Al/Ca plot) are indicated. Note that 0 mm corresponds to a depth of ~8 mm from the original surface of the specimen. (For interpretation of the references to colour in this figure legend, the reader is referred to the web version of this article.)

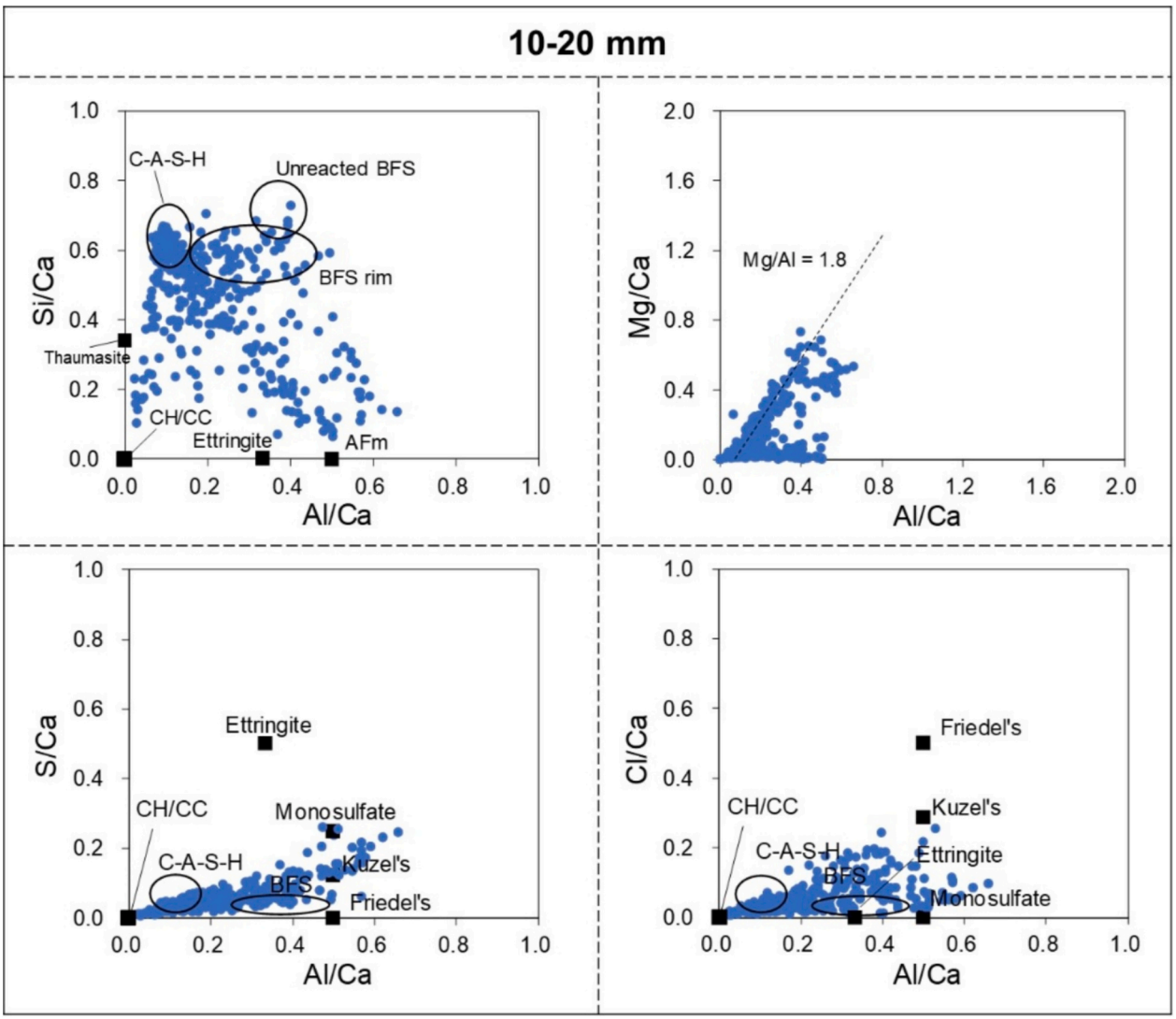


Fig. 9. (*continued*).

were frequently observed in the 0–1 mm region. Hydrates within the BFS rim, including Mg—Al LDHs and Ca—Al LDHs, also showed uptake of S and Cl. Hydrotalcite-like phases (Mg—Al LDHs) form by substituting Mg^{2+} ions in brucite-like sheets with Al^{3+} ions, resulting in positively charged Mg—Al main sheets. The interlayer spaces accommodate anions such as CO_3^{2-}, OH^-, Cl^-, and SO_4^{2-}, along with water molecules [59]. While the affinity of these phases for anions follows the order CO_3^{2-}, $OH^- > Cl^-$, SO_4^{2-}, uptake of Cl^- and SO_4^{2-} into the interlayers has also been reported [42,52,60].

The Si/Ca–Al/Ca plots (Fig. 9) obtained at 4–6 mm and 10–20 mm from the surface show that C-A-S-H in these regions remained largely unaffected by decalcification, relative to 0–1 mm. At 4–6 mm, C-A-S-H coexisted with ettringite and Friedel's salt outside BFS rims. Additionally, a small amount of CH and/or calcite, undetectable by XRD, may also be present. The S/Ca–Al/Ca plots in Figs. 9 and 10 show data points (red-circled) that have shifted slightly from the C-A-S-H cluster toward the stoichiometric composition of ettringite. This suggests the presence of sub-microscopic ettringite precipitating within C-A-S-H, which are undetectable with SEM but known to exert expansive pressure [36,61]. At 10–20 mm from the surface, no such data points for sub-microscopic ettringite were observed in the S/Ca–Al/Ca plots. Within the BFS rim, C-A-S-H was found to coexist with Ca—Al LDHs and Mg—Al LDHs (hydrotalcite-like phases) that had taken up Cl and S.

3.4.4. *Low-temperature specimens*

Figs. 12 and 13 present EDS point analysis data for the low-temperature specimens at 500× and 1500× magnification respectively. Overall, these show phase changes that were more pronounced than those observed at ambient temperature, but less pronounced than in the deep-sea. For example, the S/Ca and Cl/Ca–Al/Ca plots in Figs. 12 and 13 show that the uptake of S and Cl under low-temperature conditions resembled those in the deep-sea environment. Ettringite formation was clearly observed in the surface layer (0–1 mm), while sub-microscopic ettringite intermixed with C-A-S-H was detected at 4–6 mm from the surface. In addition, Ca—Al LDHs and Mg—Al LDHs (hydrotalcite-like phases) were detected within the BFS rims. These phases exhibited Cl and S uptake across the 0–1 mm to 10–20 mm depth range. However, hydrotalcite-like phases with higher Mg/Ca and Al/Ca contents (as seen in the deep-sea specimens) did not form under low-temperature conditions, as shown in the Mg/Ca–Al/Ca plots (Fig. 13).

Decalcification of C-A-S-H in the low-temp. specimen was also notably less severe compared to the deep-sea specimens. In areas outside the BFS rim at 0–1 mm depth, C-A-S-H remained largely unaffected by decalcification. This is indicated by the near absence of data points within the red-circled region in the Si/Ca–Al/Ca plots of Fig. 13. In contrast, many data are plotted in this region for the deep-sea specimens (Fig. 10).

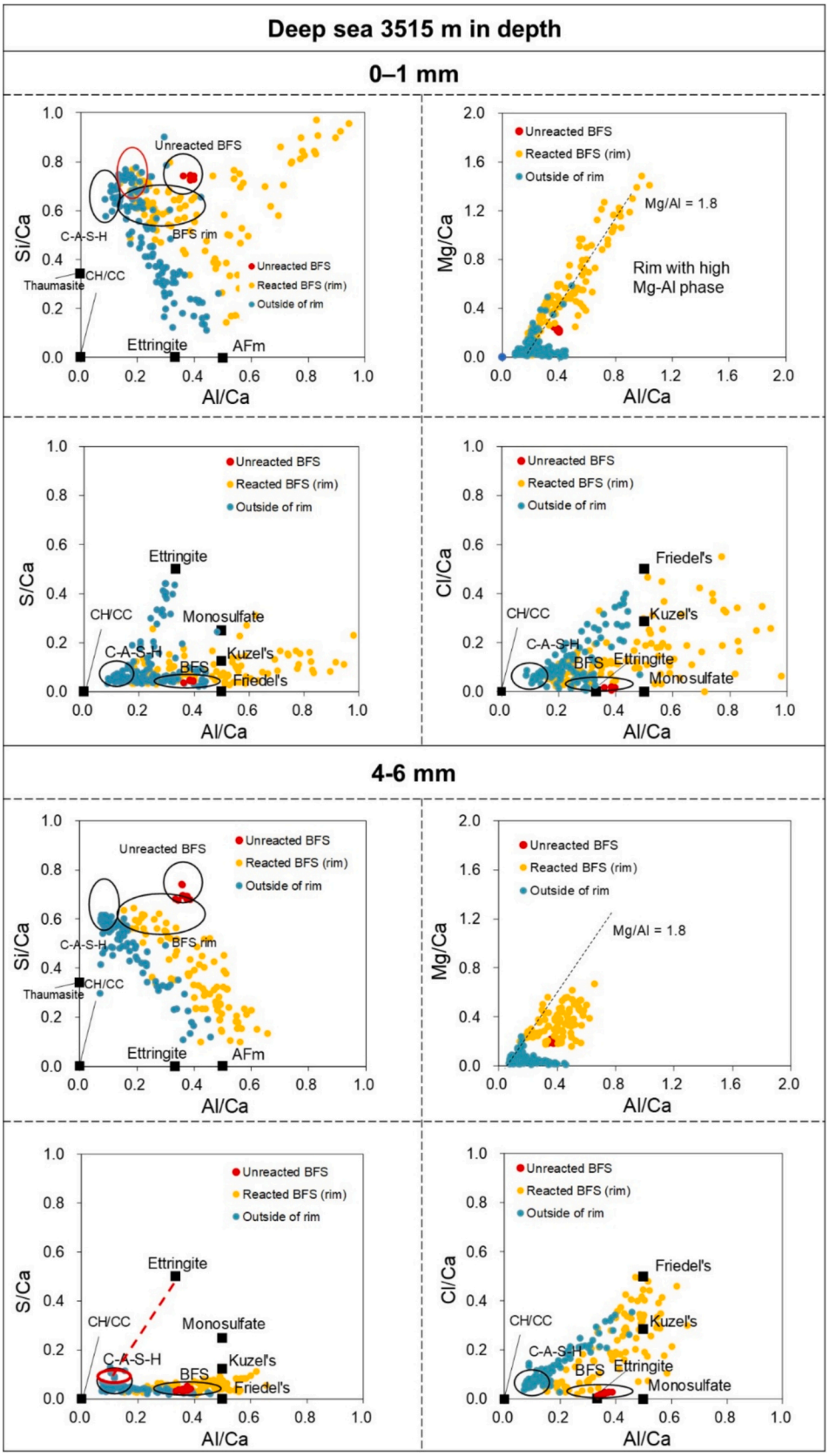


Fig. 10. EDS point analysis of deep-sea specimens at 1500× magnification. Decalcification of C-A-S-H (red-circled area in the Si/Ca–Al/Ca plot) and ettringite formation within C-A-S-H (red-circled area in the S/Ca–Al/Ca plot) are indicated. Note that 0 mm corresponds to a depth of ~8 mm from the original surface of the specimen. (For interpretation of the references to colour in this figure legend, the reader is referred to the web version of this article.)

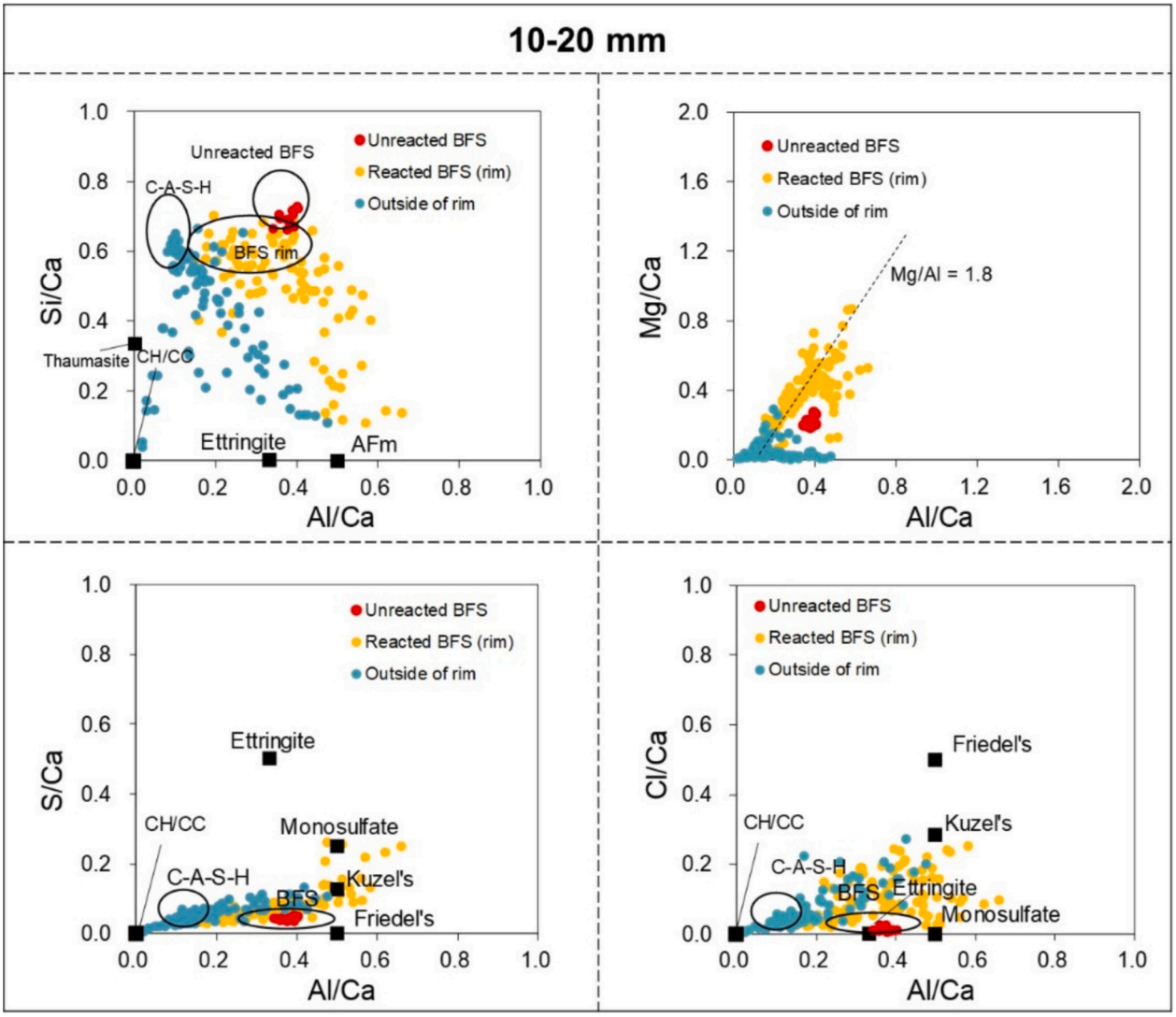


Fig. 10. (*continued*).

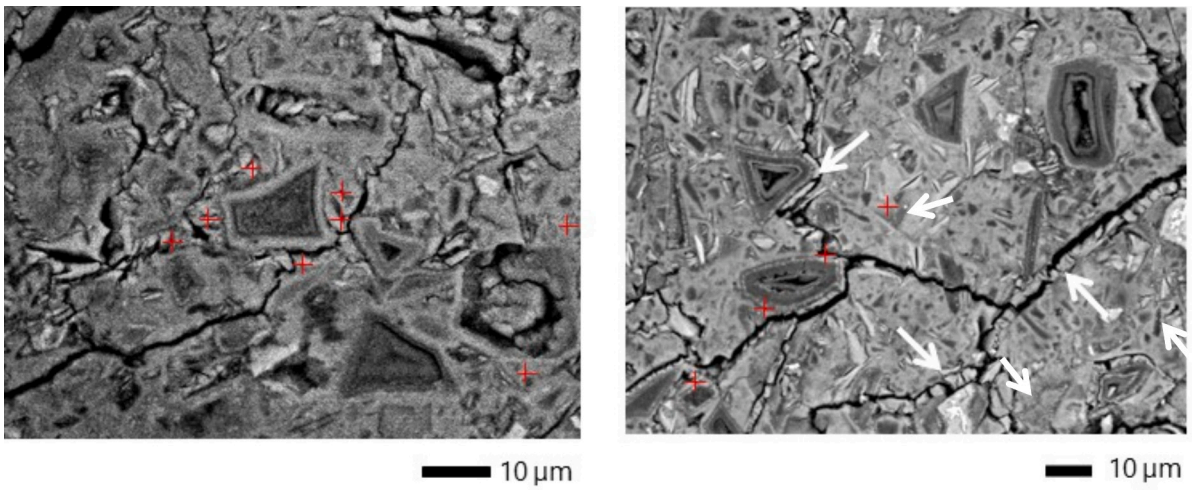


Fig. 11. BSE images showing ettringite formation in the 0–1 mm region of the deep-sea specimens. Left: Ettringite co-precipitated with C-A-S-H outside BFS rims. Right: Ettringite crystals filling cracks (arrowed).

Table 2
EDS point analysis of the locations marked with "+" in Fig. 11. Maximum, minimum, and average values are presented. The stoichiometric composition of ettringite is Al/Ca = 0.33 and S/Ca = 0.50.

	Al/Ca			S/Ca		
	Average	max	min	Average	max	min
Left	0.28	0.30	0.21	0.37	0.44	0.19
Right	0.32	0.34	0.28	0.38	0.40	0.35

3.4.5. Changes in phase zonation

Fig. 14 provides a summary of the phase zonation within the deep-sea specimens, as determined from XRD and SEM-EDS. It also highlights the differences compared to the ambient-temp. and low-temp. specimens. While this study does not provide explicit data on seawater-derived Mg zonation, the arrows in the figure are based the findings from a previous study [15,62–64], which suggests that the C-A-S-H decalcification regions align closely with those of Mg ingress.

Although thaumasite was not directly detected by SEM-EDS analysis in any of the specimens investigated in this study, the GEMS modelling results (Fig. A4) suggest that thaumasite formation becomes thermodynamically favorable under extensive seawater ingress. Given that thaumasite formation has been observed in PC-based systems under similar deep-sea conditions [12], it cannot be ruled out that thaumasite might have formed in eroded regions where material loss occurred.

3.5. Phase changes around BFS grains induced by deep-sea exposure

The multi-rim feature observed within reacted BFS (Figs. 8, 11, and 15) reflect the heterogeneous distribution of C-A-S-H, Ca—Al LDHs, and hydrotalcite-like phases. Although the resolution of SEM-EDS does not allow precise elemental quantification of each rim, the phase changes can be deduced from the findings of Li et al. [43] using focused ion beam-SEM and transmission electron microscope-EDS. Fig. 15A shows the unreacted BFS grain, reacted rims, and area outside the rim for the reference (ambient-temp. specimen, 20 mm from the surface). The innermost rim I adjacent to the unreacted BFS grain is rich in Mg and Al, predominantly forming hydrotalcite-like phases along with C-A-S-H and Ca—Al LDHs [43,53,54,65]. Beyond this, a thin brighter layer (rim II) enriched in Ca is observed, followed by rim III, which is darker and again rich in Mg and Al. The area outside the rim exhibits higher Ca and Si concentrations [43].

The dissolution and precipitation processes during the reaction of BFS are similar to those of Portland cement, beginning with incongruent surface dissolution. The energy gap for dissolution is reduced at etched pits on the particle surface, facilitating dissolution and subsequent nucleation and precipitation. The reaction front of BFS progresses inward as hydration continues [43]. Water content in BFS is lower than in cement paste, resulting in the ingress of water and anions toward the reaction front [55], while cations are released outward from the BFS grain. Among the dissolved ions, Ca ions diffuse farther from the BFS grain compared to Mg and Al ions (yellow arrows in Fig. 15A). Si ions, predominantly derived from PC, and Ca ions precipitate as C-A-S-H, forming a dense structure outside the rim [66]. Within rim III, Mg and Al concentrations increase (red arrows in Fig. 15A), resulting in the formation of hydrotalcite-like phases with a coarser morphology [43]. The reduced supersaturation caused by the precipitation of hydrotalcite-like phases draws dissolved Ca and Si ions into rim II (blue arrows in Fig. 15A), forming C-A-S-H and Ca—Al LDHs. As hydration progresses, the thickness of these rims increases, restricting water and ion diffusion to the unreacted portions. Consequently, newly dissolved Ca and Si ions are less likely to diffuse into the area outside the rim.

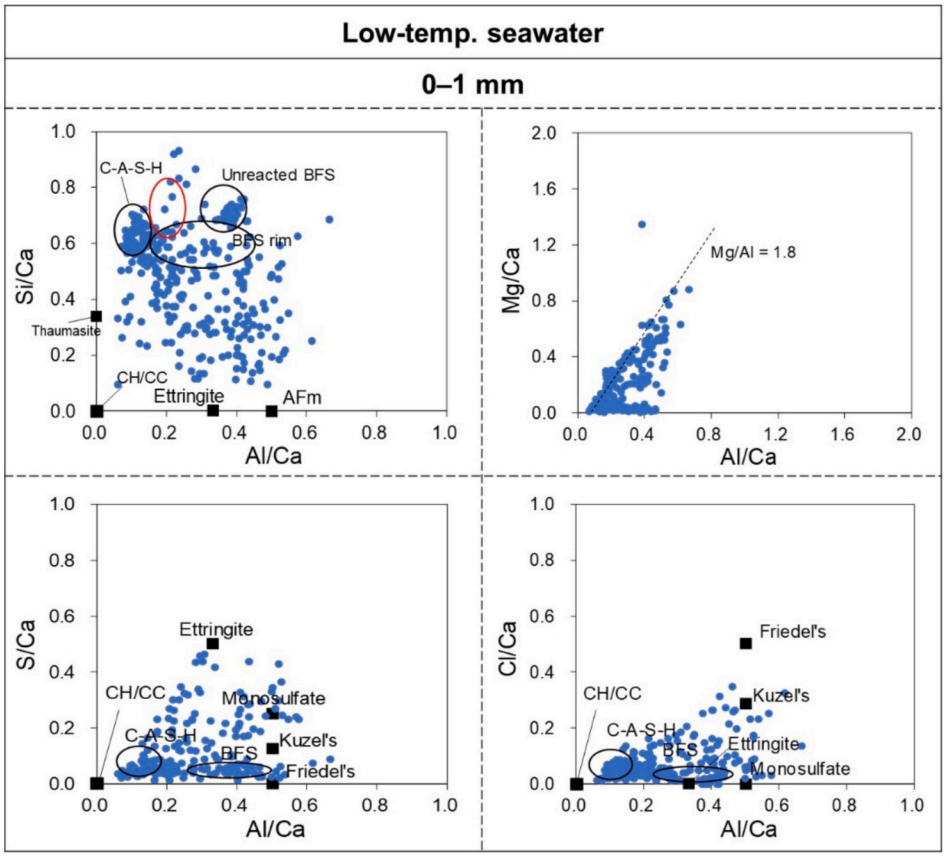


Fig. 12. EDS point analysis of low-temp. specimens at 500× magnification. Ettringite formation within C-A-S-H (red-circled area in the S/Ca–Al/Ca plot) is indicated. (For interpretation of the references to colour in this figure legend, the reader is referred to the web version of this article.)

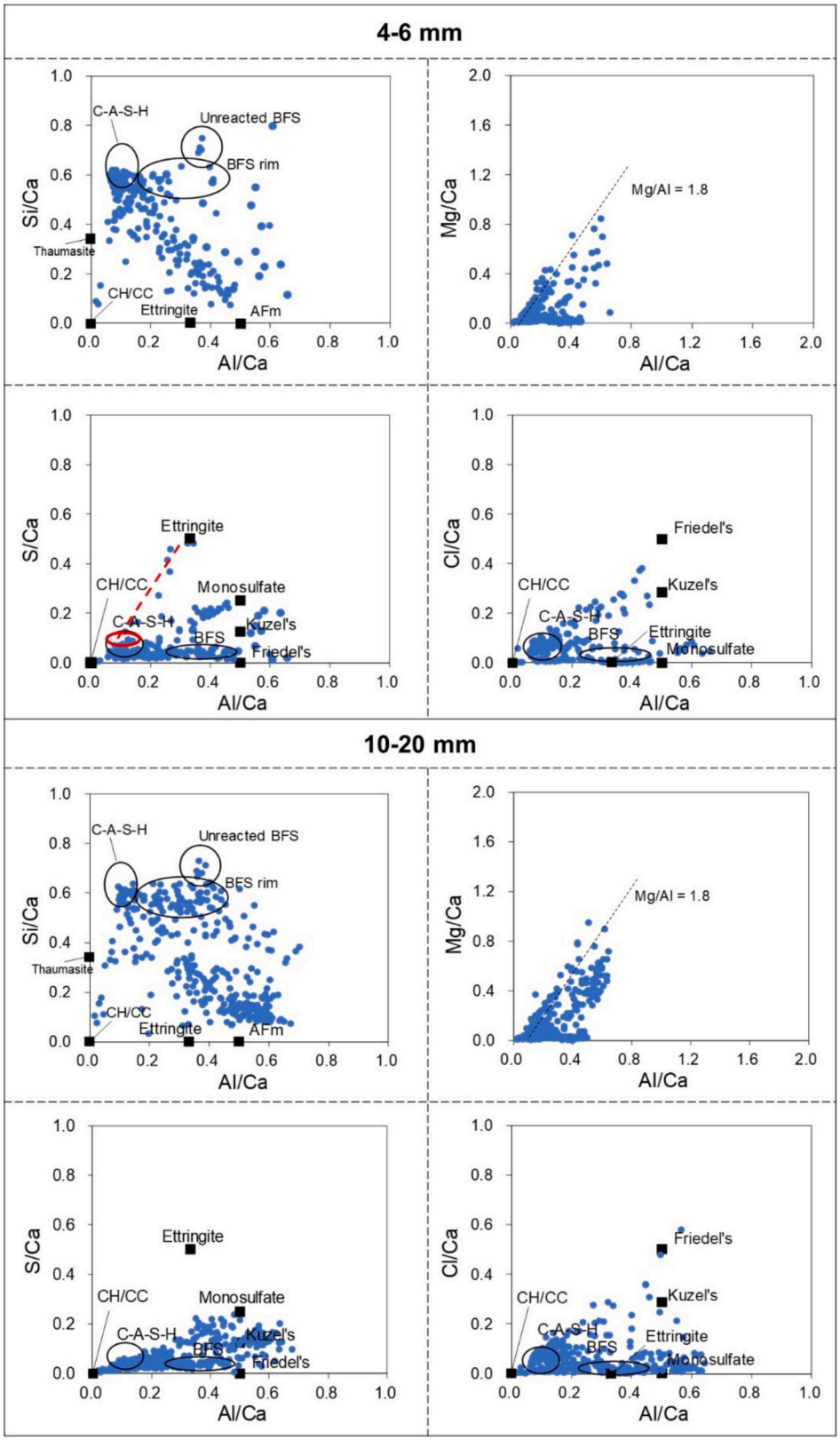


Fig. 12. (*continued*).

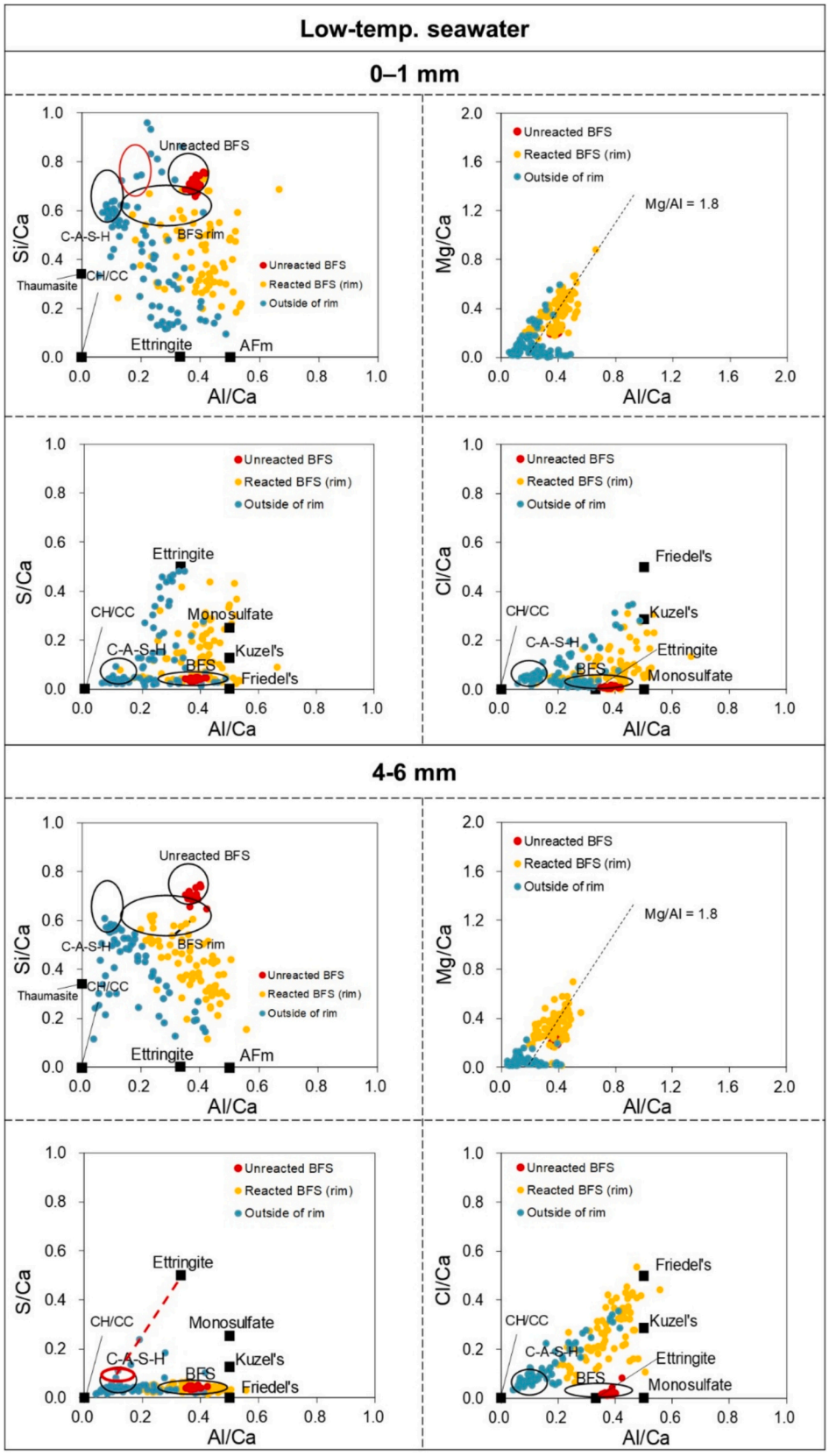


Fig. 13. EDS point analysis of low-temperature specimens at 1500× magnification. Ettringite formation within C-A-S-H (red-circled area in the S/Ca–Al/Ca plot) is indicated. (For interpretation of the references to colour in this figure legend, the reader is referred to the web version of this article.)

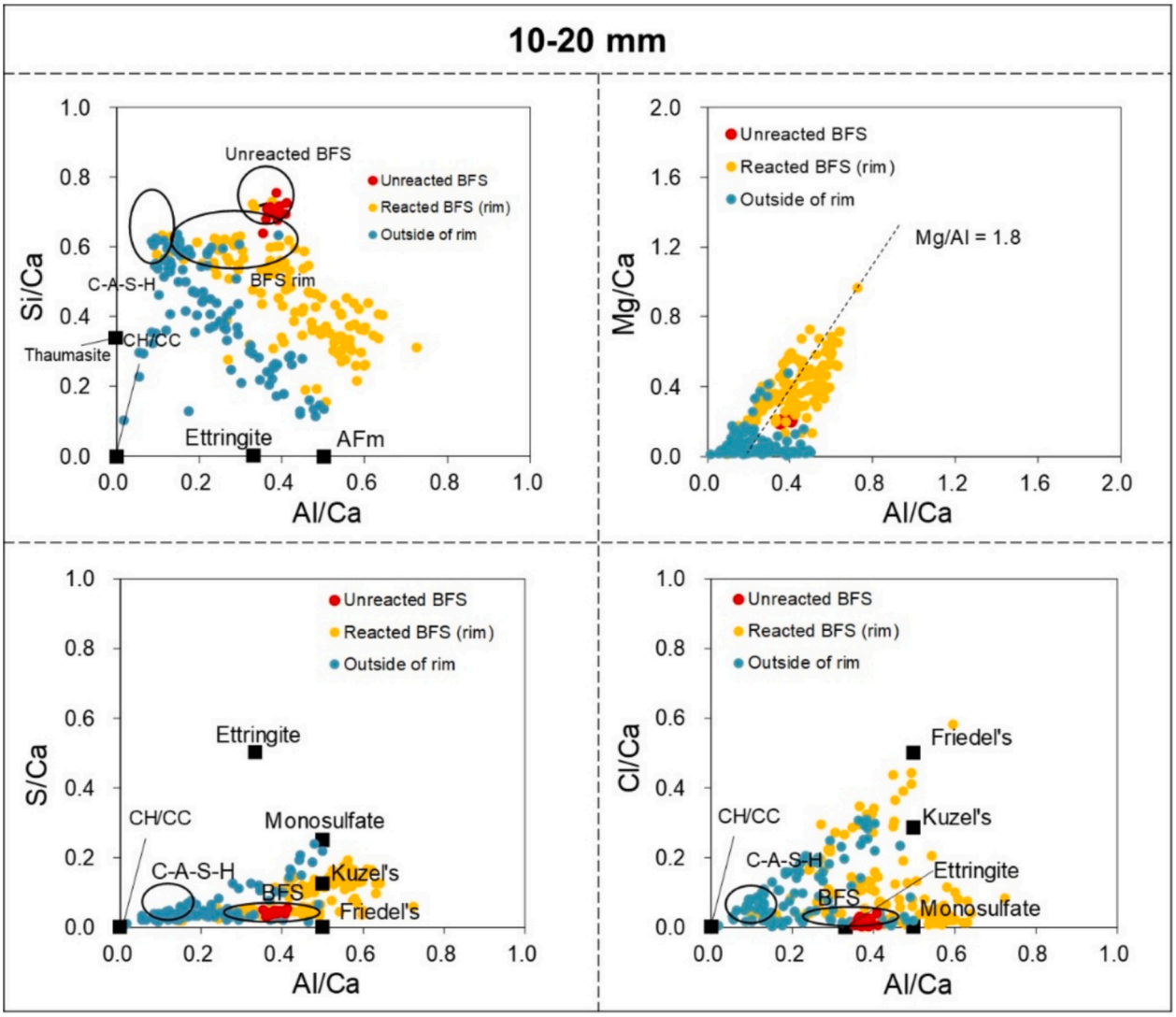
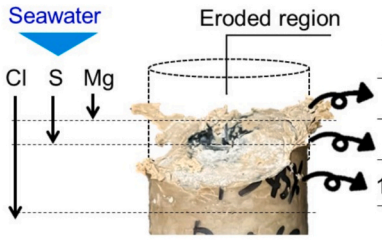


Fig. 13. (*continued*).



Location (+ 8 mm)	Phases
0–1 mm	C-A-S-H* Ett Fs Ca-Al LDHs HT
4–6 mm	C-A-S-H Ett** Fs Ca-Al LDHs HT CH
10–20 mm	C-A-S-H Ks Ca-Al LDHs HT CH

C-A-S-H*: significantly decalcified
Ett**: invisible and fine

- Ca-Al LDHs and HT contained Cl and S
- CC was detected in all areas

– : not/less observed
+ : observed

	Deep-sea	Ambient-temp.	Low-temp.
Decalcification	+	–	–
Ettringite formation	+	–	+
High Mg-Al in rims	+	–	–
Cl, S uptake in LDHs	+	–	+

Fig. 14. Phase zonation in the deep-sea specimens compared to the ambient-temp. and low-temp. specimens. Abbreviations: Ett = ettringite, Fs = Friedel's salt, Ks = Kuzel's salt, HT = hydrotalcite-like phases, CC = calcium carbonate.

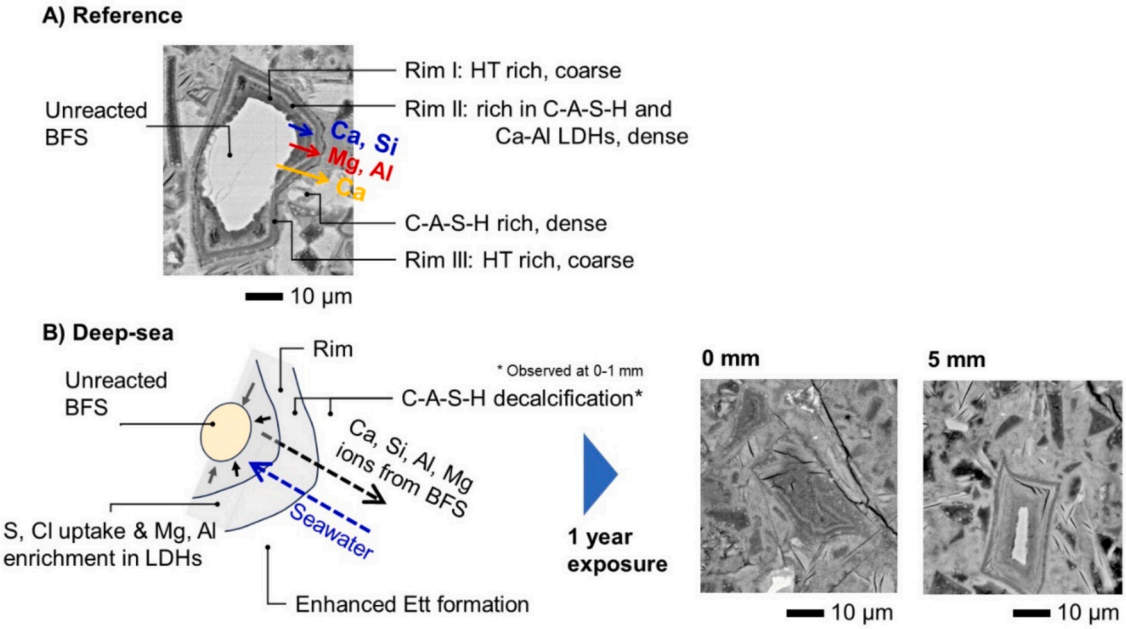


Fig. 15. Phase changes in the BFS rim and surrounding area. A) Reference: ambient-temp. specimen, 10–20 mm from the surface. B) Deep-sea specimen. Abbreviations: Ett = ettringite, HT = hydrotalcite-like phase.

Fig. 15B illustrates the phase changes observed in the deep-sea specimen. In the surface layer (0–1 mm), C-A-S-H in both the rim and the area outside exhibited significant decalcification, as shown in Figs. 9, 10, and 14. Decalcification caused by low-temperature seawater increased porosity [15], which combined with the high hydraulic pressure, allowed seawater to infiltrate the specimen fully (Section 3.2). The surface region, being most exposed to seawater, experienced accelerated dissolution of partially hydrated BFS grains. This is consistent with the BSE images in Fig. 3, where unreacted BFS grains were scarcely observed at the surface (0 mm) and were only sporadically detected at 5 mm and 20 mm of the deep-sea specimens.

Furthermore, the GEMS modelling results (Fig. A1) suggest that the additional reaction of BFS promoted by seawater ingress leads to an increase in solid volume, mainly due to ettringite formation. This secondary hydration, together with crystallization pressure generated by ettringite precipitation, likely contributed to the internal expansion and subsequent disintegration observed in the deep-sea specimens.

Dissolved Ca, Si, Mg, and Al ions from BFS grains diffused into the rim and beyond, precipitating as Mg—Al LDHs, C-A-S-H and Ca—Al LDHs, despite C-A-S-H decalcification induced by seawater ingress. Repeated cycles of dissolution and precipitation increased Mg and Al concentrations in the rim as shown in Figs. 9 and 10. Additionally, sulfate and chloride ions from the seawater were incorporated into the Ca—Al LDHs and Mg—Al LDHs (hydrotalcite-like phases).

In contrast, seawater ingress due to hydrostatic pressure was minimal in the low-temp. specimens. Although ettringite formation was observed, no significant decalcification of C-A-S-H occurred (Figs. 12 and 13). At 4–6 mm from the surface, CH was present in the low-temp. specimens but absent in the deep-sea specimens. These observations suggest that ettringite formation initiated microstructural damage in deep-sea and low-temperature environments. Additionally, the dense C-A-S-H intermixed with BFS grains in the low-temp. specimens prevented further dissolution of BFS, as evidenced by the presence of unreacted BFS grains even at 0–1 mm (Fig. 3). This also explains the lack of Mg and Al enrichment in the rim of the low-temp. specimens.

3.6. Susceptibility of BFS cement paste to deep-sea deterioration

As discussed in Section 3.5, the initiation of damage in deep-sea environments is primarily associated with ettringite formation combined with Ca leaching, which accelerates degradation. This mechanism applies to both PC-BFS and PC-based cementitious materials. The BFS45 system exhibits a higher alumina content compared to PC (see values in parentheses in Table 1). Considering the reaction rate of BFS, the SO_3/Al_2O_3 molar ratios are 0.54 for BFS45 and 0.72 for PC, based on bulk oxide compositions. Given the stoichiometric molar ratio for ettringite is 3.00 and for monosulfate is 1.00, the BFS45 exhibited a relative deficiency of SO_3 compared to Al_2O_3, stabilizing the hydrates through the formation of hydrotalcite and monosulfate. However, as discussed by Hemstad et al. [67], a fraction of Al is incorporated into C-A-S-H, reducing the amount available for AFm and AFt phase formation.

To estimate the impact of Al uptake into C-A-S-H on AFm and AFt

Table 3
Corrected SO_3/Al_2O_3 molar ratios for AFm and AFt phase formation, accounting for Al uptake into C–A-S–H. NOTE: Values are based on oxide compositions, assuming fully hydration of PC. Al/Si ratios were obtained from literature [44–47,68,69] and EDS data selected from the upper-left edge of the C-A-S-H cluster.

Specimens	Al/Si (atom%) from EDS (upper) /Literature (lower)	BFS hydration ratio (%, assumed)	Al_2O_3 uptake into C-A-S-H (mol)	Al_2O_3 available for AFm/AFt (mol)	Corrected SO_3/Al_2O_3 molar ratio for AFm/AFt
PC	7	–	0.012	0.041	0.93
	5–10	–	0.008–0.017	0.036–0.044	0.86–1.06
PC-BFS45	15	60	0.025	0.042	0.63
		100	0.032	0.060	0.50
	10–15	60	0.021–0.032	0.060–0.071	0.43–0.50
		100	0.017–0.025	0.042–0.050	0.53–0.63

phase formation, SO_3/Al_2O_3 ratios were corrected based on reference-state compositions. These corrected values, shown in Table 3, were calculated using Al/Si ratios obtained from EDS measurements of the reference specimens (i.e., ambient seawater exposure, 20 mm from the surface) in Figs. 6 and A6, as well as from published values [44–47,68,69]. In each case, EDS data were selected from the upper-left edge of the C-A-S-H cluster where the influence of phase intermixing (e.g., with hydrotalcite) is considered minimal. These reference-based estimates show that the PC-BFS system consistently exhibited lower corrected SO_3/Al_2O_3 ratios compared to PC.

Under deep-sea and low-temperature exposure conditions, EDS results showed that the Al/Si ratio in C-A-S-H ranged from 0.10 to 0.19 for PC-BFS (Figs. 9 and 12), and from 0.05 to 0.07 for PC (Fig. A6). Based on these values, the corresponding corrected SO_3/Al_2O_3 ratios were calculated as 0.43 to 0.54 for PC-BFS and from 0.86 to 0.93 for PC, assuming full hydration of PC and BFS. These findings indicate that PC-BFS is more sulfate-deficient than PC across all exposure conditions, and is predisposed to degradation through ettringite formation once pressure-induced seawater ingress occurs in deep-sea conditions. As illustrated in Fig. 15, this triggers the release of hydroxide ions to maintain electrical neutrality with the ingress of sulfate and chloride ions. The continuous exchange of these ions promotes a cycle of ettringite formation, Ca leaching, and further dissolution of BFS.

Ettringite preferentially forms outside the rim, which is richer in Ca than in the BFS rim. The S/Ca–Al/Ca plots in Figs. 10 and 13 reveal clusters extending from the C-A-S-H domain toward ettringite. These findings, coupled with SEM-EDS analysis (Fig. 11 and Table 2), suggest that sub-microscopic ettringite had formed outside the rim. These finely dispersed ettringite crystals is likely to induce stress concentration and microstructural damage to the C-A-S-H matrix.

A low temperature environment is expected to further accelerate ettringite precipitation since the solubility of ettringite decreases at lower temperatures [25]. Indeed, thermodynamic equilibrium calculations (Appendix A1, Fig. A3) show that ettringite precipitates more readily under deep-sea conditions (2 °C, 35 MPa) compared to shallow-sea conditions (20 °C, 0.1 MPa). As reported in previous studies [36,38], the solubility of ettringite decreases at lower temperatures, which increases the supersaturation level of the pore solution and consequently the crystallization pressure. This may enhance the mechanical stress exerted on the C-A-S-H matrix, contributing to microstructural damage. Although direct measurements of crystallization pressure and pore structure were not available in this study, these factors are subjects of ongoing investigation by the authors. Moreover, thermodynamic equilibrium calculations (Fig. A1) suggests that BFS can react with seawater to form ettringite (via monosulfate) and hydrotalcite-like phases. This reaction becomes particularly pronounced when seawater input exceeds a threshold, causing rapid increase in ettringite precipitation compared to PC (Fig. A2).

However, the experimentally observed differences in phase changes between the deep-sea, low-temperature seawater, and ambient-temperature seawater conditions were more pronounced than the trends predicted by thermodynamic calculations. Details are explained in Appendix A1, but while the calculated relationship between hydration phases and seawater amount showed little difference between deep-sea and ambient temperature conditions, the experimental results revealed a significant difference. This discrepancy underscores the necessity for expanding the thermodynamic datasets by including low-temperature and/or high-pressure conditions to improve predictive accuracy.

The addition of limestone fillers could be an effective strategy to mitigate the susceptibility of BFS cement-based materials to deep-sea deterioration. This approach is expected to stabilise aluminates by promoting the preferential formation of hemicarbonate and monocarbonate over monosulfate, allowing excess sulfate to be consumed as ettringite rather than being incorporated into the AFm phases [70,71]. Improved sulfate resistance with small additions of limestone powder has been reported in other studies [5,70]. The thermodynamic equilibrium calculations presented in Fig. A4 also suggest a reduction in ettringite formation under seawater ingress. On the other hand, Fig. A4 also indicates that the addition of limestone fillers could increase the amount of thaumasite formation when seawater ingress becomes extensive. Since the field exposure site used in this study is expected to be around the CCD, further investigation is needed to understand the dissolution behaviour of calcium carbonate and the stability of hemicarbonate and monocarbonate under such deep-sea conditions.

4. Conclusion

This study examined the microstructure and phase transformation of Portland cement-blast furnace slag (PC-BFS) cementitious materials after one-year exposure in a deep-sea field site at 3515 m depth. The results were compared against laboratory exposed specimens in low (2 °C) and ambient temperature seawater at atmospheric pressure (0.1 MPa), with associated water penetration and thermodynamic equilibrium calculations. The aim was to advance understanding of the degradation mechanisms in deep-sea environments, characterised by high hydraulic pressure and low temperature. The key findings are:

a) PC-BFS cement paste deteriorated more severely than PC under deep-sea conditions due to its higher Al content relative to available sulfate, making AFm phases more prone to transformation upon seawater ingress. Additionally, unreacted BFS grains reacted with infiltrating seawater, promoting additional hydration and phase changes. These reactions promoted ettringite formation (expansive), which combined with the decalcification of C-A-S-H, caused microstructural damage and deterioration.
b) Under atmospheric pressure, limited seawater penetration suppressed sulfate ingress and prevented expansion, maintaining structural integrity. In contrast, deep-sea pressure enabled full seawater infiltration, as confirmed by fluorescence tracer tests and X-μCT, with SEM-EDS and XRD analyses showing accelerated phase transformations and deterioration.

These findings highlight the limitations of PC-BFS in extreme marine conditions and the need for further material optimisation. Incorporation of limestone powder into PC-BFS is expected to stabilise aluminates and enhance resistance to seawater-induced damage. However, its effectiveness needs to be verified in deep-sea regions around and/or below the carbonate compensation depth (CCD) where carbonates become undersaturated. The thermodynamic database also needs to be expanded to better address low-temperature and high-pressure scenarios. Advancing the understanding of such deterioration mechanisms will support the development of more durable cementitious materials for deep-sea infrastructure, cold marine environments, and other challenging applications.

CRediT authorship contribution statement

Keisuke Takahashi: Writing – original draft, Investigation, Funding acquisition, Data curation, Conceptualization. **Yuichiro Kawabata:** Writing – review & editing, Investigation, Funding acquisition, Conceptualization. **Mari Kobayashi:** Writing – original draft, Investigation, Data curation. **Takafumi Kasaya:** Writing – review & editing, Resources, Funding acquisition. **Shintaro Miyamoto:** Writing – review

& editing, Formal analysis. **Hong S. Wong:** Writing – review & editing, Funding acquisition.

Funding sources

This work was partially supported by JSPS KAKENHI Grant Numbers JP23K17779, JP21H01590, JP21H01405, JP23K03987, and JRP-LEAD with UKRI (JPJSJRP20241715).

Declaration of competing interest

The authors declare that they have no known competing financial interests or personal relationships that could have appeared to influence the work reported in this paper.

Acknowledgements

We sincerely thank Professor Dr. Toshiro Yamanaka from the Tokyo University of Marine Science and Technology and Professor Dr. Mitsuyasu Iwanami from the Institute of Science Tokyo for their assistance with conducting the deep-sea field tests. We extend our heartful thanks to the captains and crews of the research vessel Yokosuka as well as to the operation team of SHINKAI 6500 for their assistance during the YK22-09C and YK23-08C cruises.

Appendix A

A.1. Phase transition modelling

Thermodynamic modelling was performed using the Gibbs Energy Minimization program package (GEM) Selektor, employing GEMS3 [72,73] and Cemdata18 [74] for calculations. The CSHQ model [75] was utilized to describe the C-S-H phases, while data for M-S-H were obtained from Ref. [76]. The compositions of PC and BFS shown in Table 1 were used as input data for the calculations. The hydrated paste was computationally titrated with 0–30 kg of seawater per 100 g of binder to predict the progressive change in phase assemblage induced by seawater penetration. For seawater composition, the default shallow-sea data pre-installed in GEMS3 were used, as there are minimal compositional differences between shallow and deep-sea seawater influencing seawater attack [12,13].

The BFS45 paste after three months of curing contained hydration products richer in Al compared to PC, but with insufficient S to stabilise Al phases as ettringite. Consequently, Al was predominantly stabilized as hydrotalcite and monosulfate, as indicated by the equilibrium phase diagram at the origin in Fig. A1. Upon seawater ingress (as indicated by the increase in X-axis values in Fig. A1), the system transitions from AFm to ettringite, accompanied by additional hydrotalcite and solid volume increase. Experimental results in this study suggested that unreacted BFS reacts with the seawater, following the path indicated by the blue arrow in Fig. A1 from B to A, leading to additional ettringite formation via AFm phases.

A similar calculation was performed for PC with identical w/b ratio and admixture content to BFS45, and the results are presented in Fig. A2. A comparison between PC and BFS45 revealed that BFS45 exhibited a rapid increase in ettringite formation and total solid volume when the seawater input exceeded a critical range of ~100–200 g per 100 g of binder. This result suggests that BFS45 is more susceptible to damage induced by seawater ingress due to accelerated ettringite formation compared to PC.

However, the limitations of the GEMS calculations were also highlighted. Fig. A1 presents the predicted phase assemblage under conditions representative of A) deep-sea, B, C) ambient pressure and temperature, and D) ambient pressure and low temperature. Despite these differences, the distinct phase changes observed experimentally using SEM-EDS and XRD were not fully captured in the predictions. For deep-sea conditions, the influence of hydraulic pressure on seawater ingress must be considered. The lack of differentiation between low-temperature and ambient-temperature under ambient pressure in the calculations underscores the need to expand the thermodynamic database to better accommodate low-temperature scenarios. High-pressure scenarios are also necessary to be considered.

The saturation index (SI) represents the degree of saturation of a chemical species and is calculated as the ion activity product divided by the solubility product. A positive log SI indicates supersaturation, implying the potential for precipitation of the species. In GEMS, log SI values are normalized by activity to reflect effective concentrations. Fig. A3 illustrates the relationship between seawater ingress and the log SI/activity of ettringite for BFS45, assuming BFS reaction rates of 60 % and 100 %. The range where log SI/activity was positive (100–6000 g seawater per 100 g binder) is shown. Under deep-sea conditions (2 °C, 35 MPa), the log SI/activity of ettringite increased more rapidly at lower seawater input levels compared to shallow-sea conditions (20 °C, 0.1 MPa). Notably, this trend was independent of the assumed BFS reaction rate.

Fig. A4 shows the effect of adding limestone powder (LSP) on the predicted phase assemblage of BFS45 paste exposed to deep-sea conditions (2 °C, 35 MPa). At 15 wt% LSP, the phase assemblage remained relatively unchanged up to 1000 g seawater addition per 100 g binder. The AFm phase is formed as monocarbonate and sulfate consumed as ettringite. This indicates superior durability compared to mixtures without LSP, where sulfate ions released by exchanging with chloride ions in AFm phases upon seawater addition lead to the ettringite formation (Fig. A1). Beyond 1000 g seawater per 100 g binder, thaumasite formation became pronounced. At 2 wt% LSP (assuming complete reaction), the AFm phase is formed as hemicarbonate and monosulfate, which uptakes chloride ions from seawater. Then, ettringite formation increased as seawater input increased. Thaumasite formation was also observed beyond 1000 g seawater per 100 g binder.

The results suggest that the addition of LSP could enhance the durability of BFS cement paste in deep-sea environments, particularly by stabilizing aluminates and reducing ettringite formation. However, there is potential for thaumasite formation at very high seawater input levels. Future studies should focus on optimizing LSP content through experiments simulating actual deep-sea conditions to maximize durability and mitigate risks associated with seawater ingress.

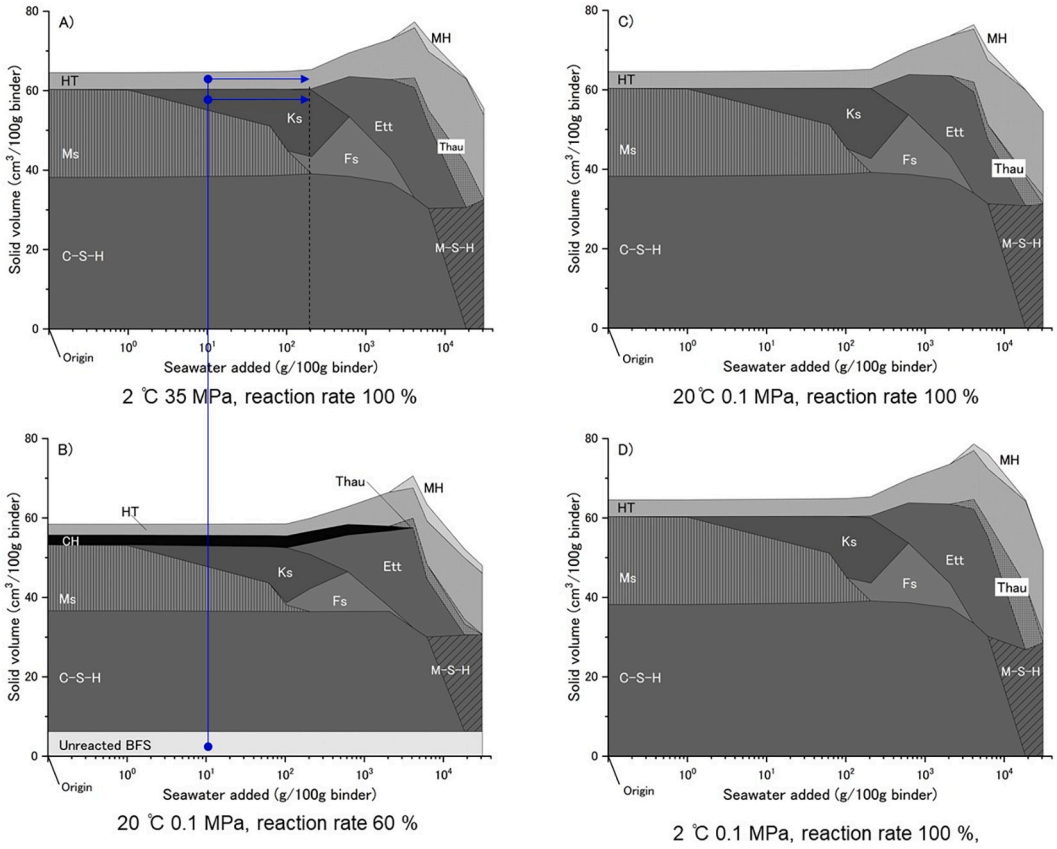


Fig. A1. Predicted phase changes in BFS45 pastes as a function of seawater ingress at different temperature and pressure conditions. A) 2 °C, 35 MPa (deep-sea condition, 3515 m depth, 100 % BFS reacted). B) 20 °C, 0.1 MPa (shallow-sea, ambient temperature, 60 % BFS reacted). C) 20 °C, 0.1 MPa (shallow-sea, ambient temperature, 100 % BFS reacted). D) 2 °C, 0.1 MPa (shallow-sea, low temperature, 100 % BFS reacted). Abbreviations: C-S-H = calcium silicate hydrate, CH = portlandite, Ms. = monosulfate, HT = OH-hydrotalcite, Ett = ettringite, Ks = Kuzel's salt, Fs = Friedel's salt, MH = brucite, Thau = thaumasite, M-S-H = magnesium silicate hydrate.

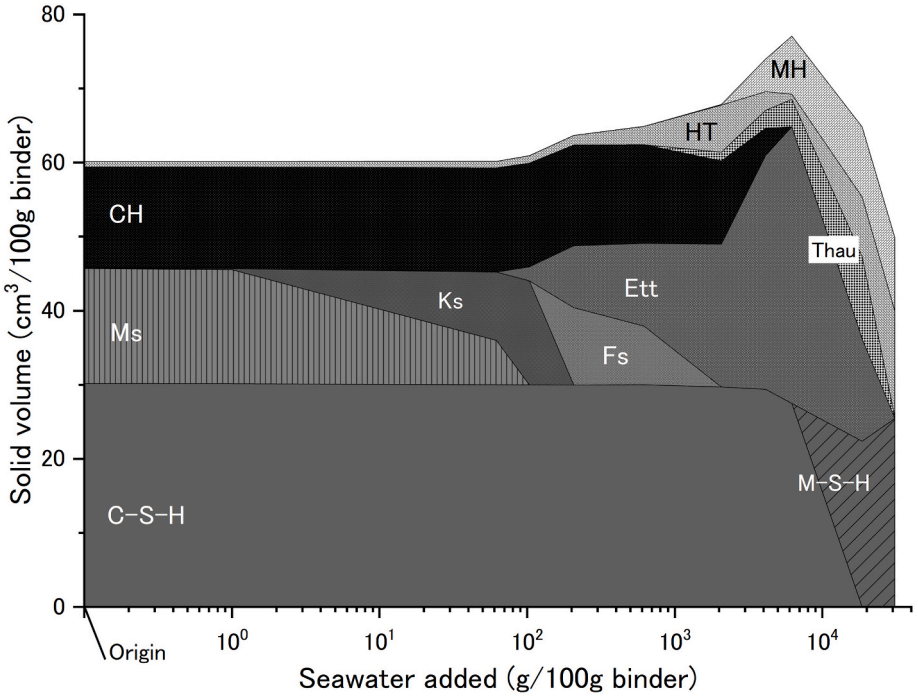


Fig. A2. Predicted phase changes of PC paste with identical w/b ratio and admixture content to BFS45, exposed to seawater ingress at 2 °C, 35 MPa. Abbreviations are consistent with Fig. A1.

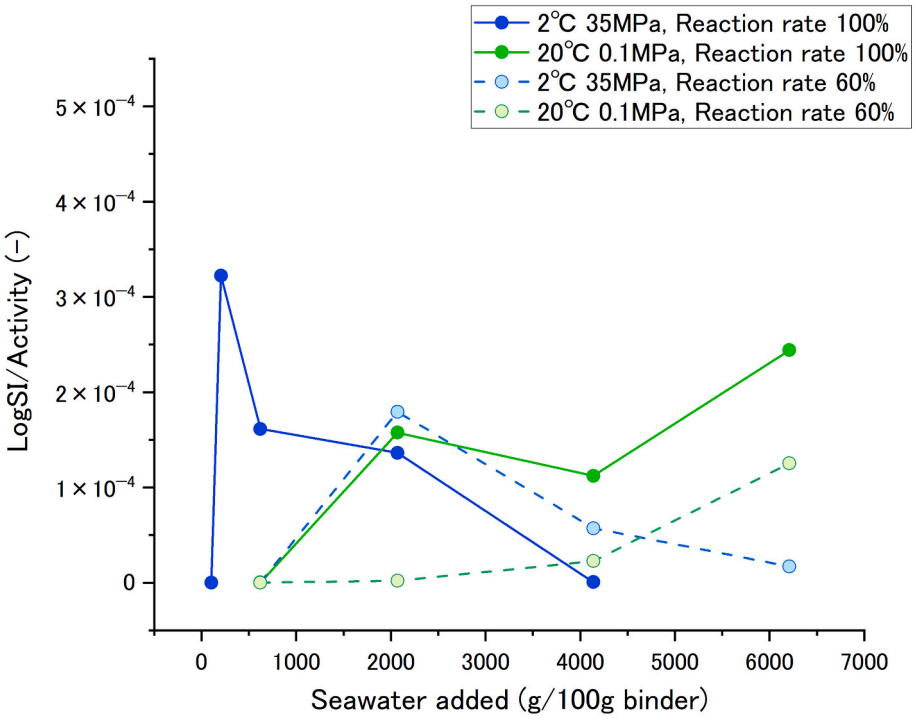


Fig. A3. Relationship between seawater ingress and the log SI/activity of ettringite in BFS45 as calculated by GEMS. The input conditions were 2 °C, 35 MPa (deep sea) and 20 °C, 0.1 MPa (shallow sea).

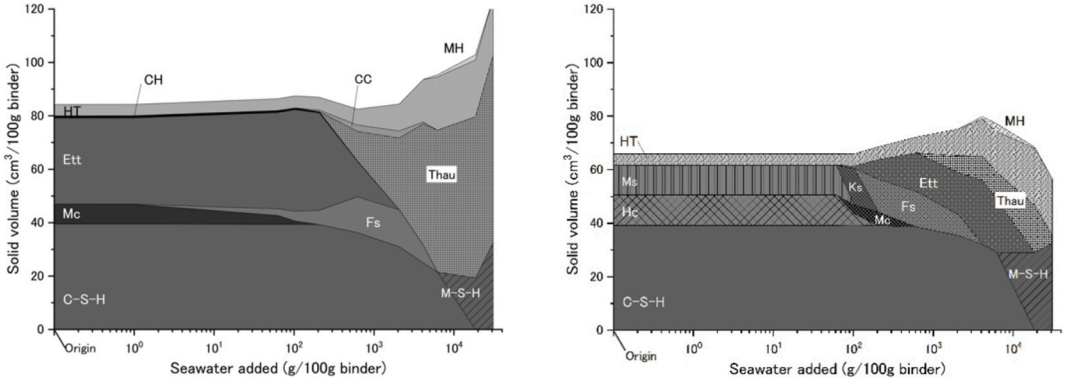


Fig. A4. Predicted phase changes of BFS45 paste with 15 wt% limestone powder (LSP) (left) and 2 wt% LSP (right) added to the total binder, and exposed to seawater ingress at 2 °C, 35 MPa. Abbreviations: Mc = monocarbonate, Hc = hemicarbonate, and others are consistent with Fig. A1.

A.2. X-μCT of water infiltration in BFS45 pastes under hydraulic pressure

As shown in Fig. 4, BFS45 paste specimens exhibited minimal water penetration (<1 mm from the surface) after 12 months under ambient pressure. These were further examined for water infiltration under hydraulic pressure using X-μCT, following the experimental procedure reported in a previous study [18]. Hydraulic pressure was manually applied using a hand pump with tap water and maintained at 20 MPa. The X-μCT system ScanXmate-D200RSS900 (Comscantecno Co., Ltd.) operated at a maximum voltage of 125 keV and an X-ray tube current of 400 μA. Radiographs were captured at 0.3° intervals, producing 1200 images. The voxel dimension was 86 μm, generating 1504 slices in the vertical direction. Differential density contrast images were processed using ImageJ software to visualize water infiltration.

Fig. A5 shows X-μCT vertical image slices of a BFS45 that were captured before pressurization (A), after 40 min at 20 MPa (B), and the differential image (C = A - B). The lighter regions in C indicate areas where water infiltrated through the top and bottom surfaces. Since water cannot penetrate through the coated surfaces, the bright appearance along the sides in the differential image is likely an artefact due to edge effects. While some dark regions remained, the centre of the specimen became lighter, indicating water penetration after 40 min at 20 MPa. The fluorescence imaging method described in Section 2.3.4 confirmed similar infiltration patterns.

Although the applied pressure was lower than the deep-sea equivalent of 35 MPa, the results clearly illustrate that water infiltration can occur through the specimen thickness under hydraulic pressure.

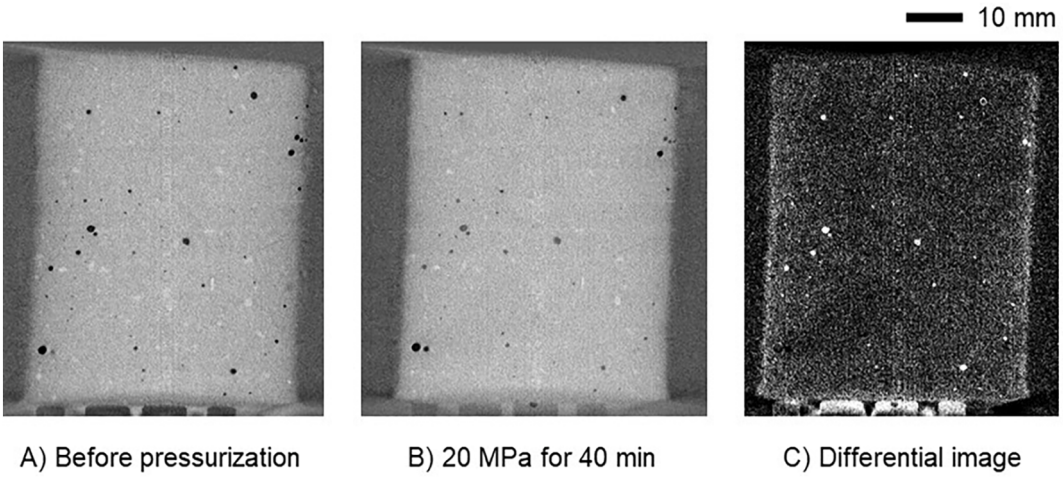


Fig. A5. Vertical image slices from X-μCT scans of a BFS45 paste. A) Before pressurization, B) after pressurization at 20 MPa for 40 min, and C) differential image between slices A and B. The lighter region in C indicate water infiltrated areas, however the bright region along the side edges is likely an artefact.

A.3. EDS results of PC specimens

Fig. A6 presents the Si/Ca vs. Al/Ca plots for the 0–1 mm and 10–20 mm regions of PC specimens after exposure under three conditions: ambient temperature seawater, low temperature seawater, and deep-sea environments. The sample preparation and EDS measurement conditions are identical to those described in the main text. The C–(A–)S–H composition was determined based on references [43, 62, 77].

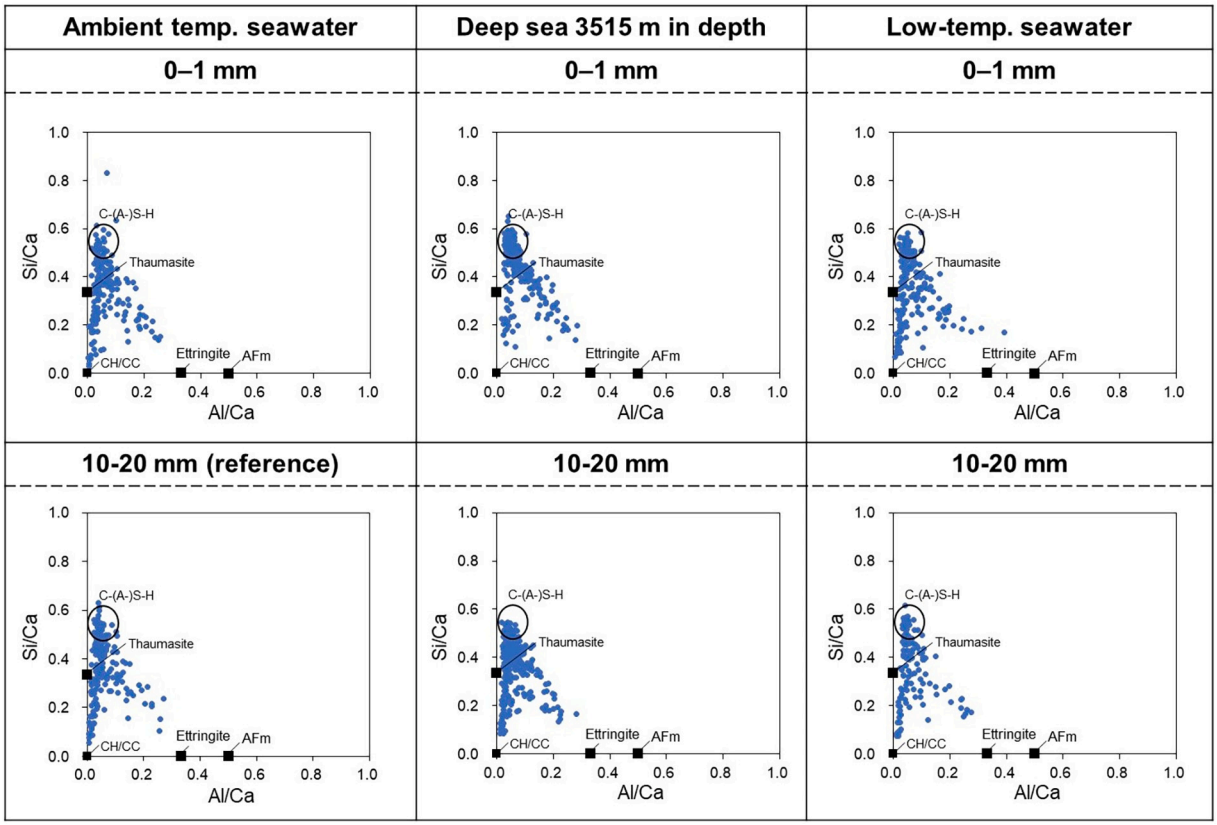


Fig. A6. Si/Ca vs. Al/Ca plots for PC specimens (0–1 mm and 10–20 mm) after exposure to ambient-temperature, deep-sea, and low-temperature conditions (at 500× magnification).

Appendix A. Supplementary data

Supplementary data to this article can be found online at https://doi.org/10.1016/j.cemconres.2025.107942.

Data availability

Data will be made available on request.

References

[1] G.J. Osborne, Durability of Portland blast-furnace slag cement concrete, Cem. Concr. Compos. 21 (1999) 11–21.
[2] J. Geiseler, H. Kollo, E. Lang, Influence of blast furnace cements on durability of concrete structures, ACI Mater. J. 92 (1995) 252–257.
[3] R.S. Gollop, H.F. Taylor, Microstructural and microanalytical studies of sulfate attack III. Sulfate-resisting Portland cement: reactions with sodium and magnesium sulfate ions, Cem. Concr. Res. 25 (1995) 1581–1590.
[4] R.S. Gollop, H.F. Taylor, Microstructural and microanalytical studies of sulfate attack, V, comparison of different slag blends, Cem. Concr. Res. 27 (1996) 1029–1044.
[5] S. Ogawa, T. Nozaki, K. Yamada, H. Hirao, R.D. Hooton, Improvement on sulfate resistance of blended cement with high alumina slag, Cem. Concr. Res. 42 (2012) 244–251.
[6] E. Güneyisi, M. Gesoğlu, A study on durability properties of high-performance concretes incorporating high replacement levels of slag, Mater. Struct. 41 (2008) 479–493.
[7] A.A. Ramezanianpour, V.M. Malhotra, Effect of curing on the compressive strength, resistance to chloride-ion penetration and porosity of concretes incorporating slag, fly ash or silica fume, Cem. Concr. Compos. 17 (1995) 125–133.
[8] L.G. Baquerizo, T. Matschei, K.L. Scrivener, M. Saeidpour, L. Wadsö, Hydration states of AFm cement phases, Cem. Concr. Res. 73 (2015) 143–157.
[9] M. Whittaker, M. Zajac, M. Ben Haha, F. Bullerjahn, L. Black, The role of the alumina content of slag, plus the presence of additional sulfate on the hydration and microstructure of Portland cement-slag blends, Cem. Concr. Res. 66 (2014) 91–101.
[10] Lea's chemistry of cement and concrete, Fourth Edition, Hewlett, P.C.. Butterworth-Heinemann, 2003.
[11] M.D.A. Thomas, P.B. Bamforth, Modelling chloride diffusion in concrete: effect of fly ash and slag, Cem. Concr. Res. 29 (1999) 487–495.
[12] M. Kobayashi, K. Takahashi, Y. Kawabata, Physicochemical properties of the Portland cement-based mortar exposed to deep seafloor conditions at a depth of 1680 m, Cem. Concr. Res. 142 (2021) 106335.
[13] M. Kobayashi, K. Takahashi, Y. Kawabata, T. Bier, Physicochemical properties of Portland cement/calcium aluminate cement/calcium sulfate ternary binder exposed to long-term deep-sea conditions, Mater. Struct. 55 (2022) 182.
[14] K. Takahashi, T. Akitou, M. Kobayashi, Changes in the physicochemical properties of calcium aluminate cement paste with high alumina content under deep seas, Constr. Build. Mater. 398 (2023) 132495.
[15] M. Kobayashi, K. Takahashi, Y. Kawabata, Deterioration of cement-based materials in low-temperature seawater, Materials 16 (2023) 5278.
[16] K. Takahashi, Y. Kawabata, M. Kobayashi, S. Gotoh, S. Nomura, T. Kasaya, M. Iwanami, Action of hydraulic pressure on Portland cement mortars - current understanding and related progress of the first-ever in-situ deep sea tests at a 3515 m depth, J. Adv. Concr. Technol. 19 (2021) 226–239.
[17] K. Takahashi, Y. Kawabata, M. Iwanami, M.T. Kobayashi, Kasaya, S. Nomura, H. Makita, In-situ deep-sea monitoring of cement mortar specimen at a depth of 3515 m and changes in mechanical properties after exposure to deep sea condition, J. Adv. Concr. Technol. 20 (2022) 254–266.
[18] Y. Kawabata, D. Takano, K. Takahashi, M. Iwanami, In situ observation for the influence of hydraulic pressure on internal damage of cement-based materials, Mater. Des. 216 (2022) 110556.
[19] S. Tsuji, E. Araki, T. Yokobiki, S. Nishida, Y. Machida, M. Zumberge, K. Takahashi, Precise tilt measurement by seafloor borehole tiltmeters at the Nankai trough subduction zone, Earth Planets Space 75 (2023) 188.
[20] K. De Weerdt, D. Orsáková, A.C.A. Müller, C.K. Larsen, B. Pedersen, M.R. Geiker, Towards the understanding of chloride profiles in marine exposed concrete, impact of leaching and moisture content, Constr. Build. Mater. 120 (2016) 418–431.
[21] E.P. Nielsen, M.R. Geiker, Chloride diffusion in partially saturated cementitious material, Cem. Concr. Res. 33 (2003) 133–138.
[22] A. Kunawisarut, Y. Kawabata, M. Iwanami, Mechanical behavior of concrete under high water pressure: water penetration as a critical factor for mechanical properties, Cem. Concr. Res. 190 (2025) 107820.
[23] Boynton, R.S. Chemistry and technology of lime and limestone, 2nd ed., Wiley-Interscience, New York, USA (1980).
[24] ChemBK. Calcium Hydroxide. Available online: https://www.chembk.com/en/chem/Calcium%20hydroxide (accessed on December 13, 2024).
[25] B. Lothenbach, T. Matschei, G. Möschner, F. Glasser, Thermodynamic modelling of the effect of temperature on the hydration and porosity of Portland cement, Cem. Concr. Res. 38 (2008) 1–18.
[26] M. Thomas, T. Bremner, Performance of lightweight aggregate concrete containing slag after 25 years in a harsh marine environment, Cem. Concr. Res. 42 (2012) 358–364.
[27] T. Kasaya, In-situ monitoring and long-term explosion test of cement mortar specimen at a deep sea condition and fundamental strength evaluation of sub-seafloor, S/V YOKOSUKA cruise report YK22-09C, Japan Agency for Marine-Earth Science and Technology (JAMSTEC) (2022), https://doi.org/10.17596/0003422.
[28] T. Kasaya, In-situ monitoring and long-term explosion test of cement mortar specimen at a deep sea condition and fundamental strength evaluation of sub-seafloor, S/V YOKOSUKA cruise report YK23-08C, Japan Agency for Marine-Earth Science and Technology (JAMSTEC) (2023), https://doi.org/10.17596/0003855.
[29] The Overseas Coastal Area Development Institute of Japan (Chapter 11), in: Technical Standards and Commentaries for Port and Harbor Facilities in Japan, 2002, 338–341 (translated from Japanese edition in 1999), http://ocdi.or.jp/en/technical-st-en (Accessed Dec. 13, 2024).
[30] JAMSTEC, SHINKAI 6500. Available online: https://www.jamstec.go.jp/e/about/equipment/ships/shinkai6500.html (accessed on December 13, 2024).
[31] M. Strasser, G. Moore, G. Kimura, Y. Kitamura, A.J. Kopf, S. Lallemant, J.O. Park, E.J. Screaton, X. Su, M.B. Underwood, X. Zhao, Origin and evolution of a splay fault in the Nankai accretionary wedge, Nat. Geosci. 2 (2009) 648–652.
[32] Dissolution of Deep-sea Carbonates, Sliter, W.V., Bé, A.W.H., Berger, W.H., Cushman Foundation for Foraminiferal Research, Volume 13 (1975) ISBN electronic:9781970168075.
[33] K. Yonamine, T. Yamaji, K. Yuichiro, A study on local cracking of concrete exposed to seawater, Cement Sci. Concr. Technol. 71 (2018) 425–431, https://doi.org/10.14250/cement.71.425.
[34] H.S. Wong, N.R. Buenfeld, Patch microstructure in cement-based materials: fact or artefact? Cem. Concr. Res. 36 (2006) 990–997.
[35] Z. Wu, H.S. Wong, C. Chen, N.R. Buenfeld, Anomalous water absorption in cement-based materials caused by drying shrinkage induced microcracks, Cem. Concr. Res. 115 (2019) 90–104.
[36] G.W. Scherer, Stress from crystallization of salt, Cem. Concr. Res. 34 (2004) 1613–1624.
[37] W. Mullauer, R.E. Beddoe, D. Heinz, Sulfate attack expansion mechanisms, Cem. Concr. Res. 52 (2013) 208–215.
[38] R.J. Flatt, G.W. Scherer, Thermodynamics of crystallization stresses in DEF, Cem. Concr. Res. 38 (2008) 325–336.
[39] D. Le Cornec, O. Wang, L. Galoisy, G. Renaudin, L. Izoret, G. Calas, Green effect in slag cement materials, Cem. Concr. Compos. 84 (2017) 93–98.
[40] Garcia, H. E., R. A. Locarnini, T. P. Boyer, J. I. Antonov, O.K. Baranova, M.M. Zweng, J.R. Reagan, D.R. Johnson, World Ocean Atlas 2013, Volume 3: Dissolved Oxygen, Apparent Oxygen Utilization, and Oxygen Saturation. S. Levitus (Ed.), A. Mishonov (Technical Ed.), NOAA Atlas NESDIS 75, 27.
[41] J.H.P. Van Aardt, S. Visser, Thaumasite formation: a cause of deterioration of Portland cement and related substances in the presence of sulphates, Cem. Concr. Res. 5 (3) (1975) 225–232.
[42] E. Bernard, W.J. Zucha, B. Lothenbach, U. Mäder, Stability of hydrotalcite (mg-Al layered double hydroxide) in presence of different anions, Cem. Concr. Res. 152 (2022) 106674.
[43] B. Li, Q. Li, W. Chen, Spatial zonation of a hydrotalcite-like phase in the inner product of slag: new insights into the hydration mechanism, Cem. Concr. Res. 145 (2021) 106460.
[44] I.G. Richardson, The nature of C-S-H in hardened cements, Cem. Concr. Res. 29 (1999) 1131–1147.
[45] Mueller, U., Lundgren, M., Babaahmadi, A., Hydration of concrete binders blended with ground granulated blast furnace slag, fly ash and metakaolin, CBI Report 2017:6, ISBN: 978-91-980851-6-7.
[46] R. Snellings, A. Machner, G. Bolte, H. Kamyab, P. Durdzinski, P. Teck, M. Zajac, A. Muller, K. De Weerdt, M. Ben Haha, Hydration kinetics of ternary slag-limestone cements: impact of water to binder ratio and curing temperature, Cem. Concr. Res. 151 (2022) 106647, https://doi.org/10.1016/j.cemconres.2021.106647.
[47] R. Taylor, I.G. Richardson, R.M.D. Brydson, Composition and microstructure of 20-year-old ordinary Portland cement–ground granulated blast-furnace slag blends containing 0 to 100% slag, Cem. Concr. Res. 40 (2010) 971–983.
[48] C. Jiang, K. Li, J. Zhang, Q. Qin, Z. Liu, M. Sun, Z. Wang, W. Liang, Effect of MgO/Al2O3 ratio on the structure and properties of blast furnace slags: a molecular dynamics simulation, J. Non-Cryst. Solids 502 (2018) 76–82.
[49] A.M. Harrisson, N.B. Winter, H.F.W. Taylor, Microstructure and microchemistry of slag cement pastes, MRS Online Proc. Libr. 86 (1986) 199.
[50] B. Li, S. Zhang, Q. Li, N. Li, B. Yuan, W. Chen, H.J.H. Brouwers, Q. Yu, Uptake of heavy metal ions in layered double hydroxides and applications in cementitious materials: experimental evidence and first-principle study, Constr. Build. Mater. 222 (2019) 96–107.
[51] M. Ben Haha, B. Lothenbach, G. Le Saout, F. Winnefeld, Influence of slag chemistry on the hydration of alkali-activated blast-furnace slag – part II: effect of Al_2O_3, Cem. Concr. Res. 42 (2012) 74–83.
[52] A. Machner, M. Zajac, M. Ben Haha, K.O. Kjellsen, M.R. Geiker, K. De Weerdt, Chloride-binding capacity of hydrotalcite in cement pastes containing dolomite and metakaolin, Cem. Concr. Res. 107 (2018) 163–181.
[53] R. San Nicolas, S.A. Bernal, R.M. De Gutiérrez, J.S.J. Van Deventer, J.L. Provis, Distinctive microstructural features of aged sodium silicate-activated slag concretes, Cem. Concr. Res. 65 (2014) 41–51, https://doi.org/10.1016/j.cemconres.2014.07.008.
[54] C. Famy, K.L. Scrivener, A.K. Crumbie, What causes differences of C-S-H gel grey levels in backscattered electron images? Cem. Concr. Res. 32 (2002) 1465–1471.
[55] I.G. Richardson, G.W. Groves, Microstructure and microanalysis of hardened cement pastes involving ground granulated blast-furnace slag, J. Mater. Sci. 27 (1992) 6204–6212.
[56] I.G. Richardson, G.W. Groves, The structure of the calcium silicate hydrate phases present in hardened pastes of white Portland cement/blast-furnace slag blends, J. Mater. Sci. 32 (1997) 4793–4802.
[57] H.S. Wong, N.R. Buenfeld, Monte Carlo simulation of electron-solid interactions in cement-based materials, Cem. Concr. Res. 36 (2006) 1076–1082.

[58] I.G. Richardson, A.R. Brough, G.W. Groves, C.M. Dobson, The characterization of hardened alkali-activated blast-furnace slag pastes and the nature of the calcium silicate hydrate (C-S-H) phase, Cem. Concr. Res. 24 (1994) 813–829.
[59] S. Miyata, Anion-exchange properties of hydrotalcite-like compounds, Clay Clay Miner. 31 (1983) 305–311.
[60] A. Machner, M. Zajac, M. Ben Haha, K.O. Kjellsen, M.R. Geiker, K. De Weerdt, Stability of the hydrate phase assemblage in Portland composite cements containing dolomite and metakaolin after leaching, carbonation, and chloride exposure, Cem. Concr. Compos. 89 (2018) 89–106.
[61] C. Yu, W. Sun, K. Scrivener, Mechanism of expansion of mortars immersed in sodium sulfate solutions, Cem. Concr. Res. 43 (2013) 105–111.
[62] K. De Weerdt, H. Justnes, M.R. Geiker, Changes in the phase assemblage of concrete exposed to sea water, Cem. Concr. Compos. 47 (2014) 53–63.
[63] U.H. Jakobsen, K. De Weerdt, M.R. Geiker, Elemental zonation in marine concrete, Cem. Concr. Res. 85 (2016) 12–27.
[64] K. De Weerdt, E. Bernard, W. Kunther, M.T. Pedersen, B. Lothenbach, Phase changes in cementitious materials exposed to saline solutions, Cem. Concr. Res. 165 (2023) 107071.
[65] D. Hadley, W. Dolch, S. Diamond, On the occurrence of hollow-shell hydration grains in hydrated cement paste, Cem. Concr. Res. 30 (2000) 1–6.
[66] J. Skibsted, R. Snellings, Reactivity of supplementary cementitious materials (SCMs) in cement blends, Cem. Concr. Res. 124 (2019) 105799.
[67] P. Hemstad, B. Lothenbach, K. De Weerdt, Distribution of sulphate and aluminium in hydrated cement pastes, Cem. Concr. Res. 180 (2024) 107467.
[68] I.G. Richardson, J.G. Cabrera, The nature of C-S-H in model slag-cement, Cem. Concr. Compos. 22 (2000) 259–266.
[69] E. L'Hôpital, B. Lothenbach, D.A. Kulik, K. Scrivener, Influence of calcium to silica ratio on aluminium uptake in calcium silicate hydrate, Cem. Concr. Res. 85 (2016) 111–121.
[70] D.D. Higgins, N.J. Crammond, Resistance of concrete containing GGBS to the thaumasite form of sulfate attack, Cem. Concr. Compos. 25 (2003) 921–929.
[71] T. Matschei, B. Lothenbach, F.P. Glasser, The AFm phase in Portland cement, Cem. Concr. Res. 37 (2007) 118–130.
[72] D.A. Kulik, T. Wagner, S.V. Dmytrieva, G. Kosakowski, F.F. Hingerl, K. V. Chudnenko, U.R. Berner, GEM-Selektor geochemical modelling package: revised algorithm and GEMS3K numerical kernel for coupled simulation codes, Comput. Geosci. 17 (2013) 1–24.
[73] T. Wagner, D.A. Kulik, F.F. Hingerl, S.V. Dmytrieva, GEM-Selektor geochemical modeling package: TSolMod library and data interface for multicomponent phase models, Can. Mineral. 50 (2012) 1173–1195.
[74] B. Lothenbach, D.A. Kulik, T. Matschei, M. Balonis, L. Baquerizo, B. Dilnesa, G. D. Miron, R.J. Myers, Cemdata18: a chemical thermodynamic database for hydrated Portland cements and alkali-activated materials, Cem. Concr. Res. 115 (2019) 472–506.
[75] D.A. Kulik, Improving the structural consistency of C-S-H solid solution thermodynamic models, Cem. Concr. Res. 41 (2011) 477–495.
[76] D. Nied, K. Enemark-Rasmussen, E. L'Hopital, J. Skibsted, B. Lothenbach, Properties of magnesium silicate hydrates (M–S-H), Cem. Concr. Res. 79 (2016) 323–332.
[77] P. Faucon, A. Delagrave, J.C. Petit, C. Richet, J.M. Marchand, H. Zanni, Aluminum incorporation in calcium silicate hydrates (C−S−H) depending on their ca/Si ratio, J. Phys. Chem. B 103 (37) (1999) 7796–7802.